GBT Memorandum No. 271

DISTORTIONS OF THE GBT BEAM PATTERN DUE TO SYSTEMATIC DEFORMATIONS OF THE SURFACE PANELS

Frederic R. Schwab and Todd R. Hunter

November 12, 2010

Abstract. The recent improvements in the small-scale surface accuracy of the GBT have warranted a detailed reexamination of the expected performance of the surface panels. Here we describe calculated, predicted distortions of the GBT beam pattern. These calculations are intended to model the effects of expected systematic deformations of the surface panels of the primary mirror. Specifically, we consider the effects of the gravitational sag of individual surface panels, front-to-back thermal gradients, and panel mold errors. We compare the modeled systematic patterns of surface distortion with the measured (holographically derived) surface error distribution, and we compare the measured beam pattern with the calculated model beam patterns. We find that under most observing conditions, thermal gradients are the major contributor to surface panel deformations, predominating over gravitational error and panel mold error. We estimate that the aggregate contribution to total surface r.m.s. from individual (systematic) panel deformation ranges from 40 to 100 microns, depending on environmental conditions.

1. Introduction. In this memorandum we describe predicted distortions of the GBT beam pattern, derived through calculation. The calculations are intended to model the effects of expected systematic deformations of the surface panels of the primary mirror. Specifically, we consider the effects of the gravitational sag of individual surface panels, front-to-back thermal gradients through the panels, and panel mold errors (which, in fact, were designed in). Finite-element models (FEMs) of the gravitational and thermal errors were developed in the early 1990s by the main contractor for the GBT. (The contractor also developed a finite-element model of the telescope as a whole, both alidade and tipping structure; but here we are concerned only with panel-scale effects, which were modeled separately from the large-scale effects.) The panel mold errors are due to having fabricated the forty-four panel tiers with the use of only sixteen tooling fixtures (or "molds"); this was done to save money. The finite-element modeled effects are described in §§2–4 below, and the mold errors in §5.

In §6 the calculated, combined effects of the these types of error on the antenna beam pattern are described. And in §7 we compare the calculated model beam patterns with the measured GBT antenna beam pattern and compare holographic maps of the surface error distribution with the model patterns of distortion.

2. Finite-Element Models of the Gravitational Distortion of Panels. Finite-element models of thermal, gravitational, and wind effects on individual panels were developed during the antenna design phase by the main contractor, Radiation Systems, Inc., (RSi) and are described in a 1992 report [**1**]. The ANSYS (Version 4.4) FEM package was used for that analysis. The primary mirror of the GBT is composed of 2004 trapezoidal aluminum panels, arranged in forty-four tiers concentric with respect to the axis of revolution of the design paraboloid. Each panel is supported at the four corner points. The panel support points are adjustable by motorized linear actuators. There are 2209 actuators, located at the panel intersections, each controlling, typically, four adjacent panel corners. The panels are of a "skin and rib" design. Panels are each approximately 2.5 meters in length (more precisely, 2.542 meters in arc length, measured in the radial direction) and are typically about two meters in width. The panel skins have been stretch-formed and are bonded with epoxy adhesive to an aluminum frame consisting of zee-shaped circumferential and radial ribs (also stretch-formed). The number of radial ribs (either 5, 7, or 9) varies from tier to tier. See Figure 1.

The FEM calculations modeled the surface errors over a rectilinear nodal grid consisting of either 135 points (for 5-rib panels), 195 points (for 7-rib panels), or 255 points (for 9-rib panels). The r.m.s. values quoted in [**1**] are actually standard deviations (i.e., root-mean-square deviations from the sample mean). For gravitational errors, it is assumed that the panel is supported horizontally and is subject to 100% gravitational load.

To the best of our knowledge, the full numerical results of the finite-element modeling were never transmitted directly to NRAO in tabular form. The results were only summarized in the contractor's report. However, for the case of the gravitational error calculations, the numerical grid values are recoverable from CMM measurement data files that were provided us; this is because those data came in two forms: the raw data file, and a "gravity-corrected" version thereof.

Plots of the finite-element model of the panel gravitational deflections are shown, for each tier, in Figure 2. Here we show a continuous representation of the surface error, calculated by interpolation using the so-called radial basis function method [**2**]. The design specification limit for a horizontally supported panel is four mils ($\sim$100 μm) standard deviation; in fact all panels are under three mils ($\sim$75 μm) standard deviation, according to the model prediction, with the exception of the Tier 31 panels, which come in at 3.1 mils.

Figure 3 shows, in the left-hand column, the overall pattern of gravitational errors over the entire primary surface, for antenna elevation angles of 5°, 44°, and 90°. (The 44° elevation corresponds to the elevation, at Green Bank, of the Galaxy 28 geostationary satellite whose beacon was used for many of the holography mapping observations.) The corresponding beam patterns at 11.7 GHz (the frequency used for holography) are shown in the right-hand column. Figure 4 (upper panel) shows the standard deviation of the gravity error for panels within each of the forty-four tiers.

3. Panel Distortion due to Thermal Gradients. Thermally induced antenna deformations are a concern in multiple aspects of the design of any radio telescope that is intended for use at millimeter wavelengths [**3**]. In the present discussion, however, we are concerned only with the panel-scale effects. For the surface panels of the GBT primary reflector, two effects were modeled in detail: first, the linear growth of panels in response to a change in temperature uniform throughout the structure; and, second, the effect of a thermal gradient between the panel front surface and the back-side of the panel rib structure.

The linear growth is straightforward to model, and here the relevant design parameter is the width of the gap between panels. If the gap closes up in response to solar heating, then the panel skins may interfere and buckle up. Gaps which become too wide in response to cooling will cause excessive scattering. The nominal gap width for the GBT primary surface panels is 2 mm.

In order to control focal heating, the GBT main surface panels are painted white, with a solar-diffusing paint [**4**], [**5**]; this choice also serves to keep the panel gaps within the acceptable range. The paint which was chosen is a modern formulation of the so-called *Triangle No. 6* (from Triangle Coatings, Inc.) which has been used since the 1960s on many NASA and NRAO antennas. von Hoerner [**6**] in Green Bank compared measurements on bare and coated aluminum surface plates and found temperature differences as high as 40 °C, "the unpainted aluminum surface goes in sunshine easily up to 70 °C at an air temperature of 30 °C, or $\Delta T = 40\,^\circ$C above air; whereas the white-painted surface goes only to $\Delta T = 5\,^\circ$C above air" [**7**].

The FEM calculation of thermal error assumes a 2 °C thermal gradient from the front side of the panel to the back; here, we define the gradient in the sense $\Delta T \equiv T_{\rm front} - T_{\rm back}$. A negative ΔT would be typical of clear sky nighttime conditions, with the panel skin colder than the ribs; and a positive ΔT would be characteristic of sunny, daytime conditions. Figure 4 (lower panel) shows the standard deviation of the thermal error for panels within each of the forty-four tiers. Figure 5 is a reproduction of a figure from the contractor's report [**1**] illustrating the thermal FEM for a Tier 26 panel. For these calculations a linear gradient was assumed. The panel skins are bonded to ribs with epoxy glue—we do not know whether the poor thermal conductivity of this glue was taken into account in the finite-element modeling.

A temperature gradient ΔT in the approximate range of $-1\,^\circ$C to $-2\,^\circ$C would be characteristic of benign nighttime observing conditions. For $\Delta T < 0$ the panel deformation Δz is negative, as with the gravitational distortion. Note that a positive ΔT, as would be expected during daytime conditions, could act to cancel out the gravitational deformation.

To our knowledge, full tabular results from the RSi thermal gradient finite-element modeling were never received by NRAO. So, in order to model the panel thermal gradient effect on the antenna beam pattern, we developed a radial basis interpolation scheme which was able (based on just the locations of the peak and corner nodes) to suitably reproduce the pattern shown in the contour plot of Figure 5. Then, assuming the location of the peak error to be at the panel centroid, and the r.m.s. distortion to be as given in the RSi table of [**1**], the same interpolation scheme as used for the Tier 26 panels was used for each of the other tiers. Plots of the finite-element model, approximated in that form, of the panel thermal deflections due to a $-2\,^{\circ}$C gradient are shown, for each tier, in Figure 6. Figure 7 shows a simulation of the 11.7 GHz beam pattern which would result from a $-2\,^{\circ}$C thermal gradient at every surface panel.

As shown in Figure 4, for $\Delta T = 2\,^{\circ}$C all panel tiers have thermal distortion standard deviations below $\sim$4 mils. The original error budget for the GBT panels allocated 3 mils, thermal; 4 mils, gravitational. Under negotiation with the contractor, that budget was later revised to 4 mils, thermal; 3 mils, gravitational.

4. Wind. RSi also included results on finite-element modeling of wind loading on the surface panels in their 1992 report, [**1**]. The calculated pattern of deformation due to wind loading is similar to that of gravitational loading. According to their calculations, wind speeds up to seven meters per second should cause no more than two mil ($\sim$50 μm) r.m.s. panel deflection.

On the subject of wind, von Hoerner includes in [**6**, §I.5] a section titled *Temperature Equalization from Wind*. This pertains to the thermal equalization of panel skin and ribs. With a prototype panel for the (proposed) 65-m Telescope, mounted near ground level, he studies the balance between radiative heat exchange with the surroundings; and convective heat exchange, assumed to be linear with wind velocity. From measurements using three 2-speed fans to blow wind at the panel, he calculates that the two effects become equalized at a certain wind speed v_0, which is approximately 3.8 miles per hour ($\sim$1.7 m/s). (The thirteen measurements were taken both in full sunshine and during clear nights.) We can probably expect that the GBT thermal performance is enhanced somewhat by light wind.

We will not give further consideration to wind loading in this report, because for high-frequency observing with the GBT, the pointing performance has probably already deteriorated once the wind-loading effect on panel figure becomes significant.

5. Designed-In Panel Mold Errors. As noted above, the primary reflecting surface of the GBT is composed of forty-four panel tiers. Panels within each tier are designed to identical dimensional specifications. The change of curvature of the design paraboloid from tier to tier is gradual enough that it was possible to reduce the required number of tooling fixtures (or "molds") from forty-four to sixteen and still meet the specified panel manufacturing accuracy of 3 mils r.m.s. (see [**8**], [**9**]).

Because of this compromise, all but eight of the forty-four panel tiers have some designed-in error. The maximum of these errors is 90 μm, and the average of the tier r.m.s. errors is $\sim$18 μm. The panel mold allocation scheme is described in further detail in Appendix A of PTCS Project Note No. 59.

Individual plots of the designed-in panel mold error for each tier are shown in Figure 8. Figure 9 shows the 11.7 GHz error beam pattern which would correspond to mold errors alone. There, the near-in sidelobes are very apparent and quite severe. Fortunately, in the presence of other errors, these features become greatly diminished, as is shown in our next section.

6. Simulations of the GBT Beam Pattern Including All Modeled Effects. Simulations of the GBT beam pattern which include all the modeled effects are shown in Figures 10–13. Figure 10 shows the predicted beam pattern at 11.7 GHz, which is the frequency of the satellite beacon signals used in the holographic mapping campaign of 2009. In the upper panels, the high sidelobe levels are due to the combination of gravitational sag with thermal "cupping" caused by the negative temperature gradient.[1] In the bottom panel, a positive temperature gradient is assumed, and here

[1]The term *cupping* is borrowed from a paper by MacDonald *et al.* [**10**] describing design alternatives for the primary mirror of the Cornell–Caltech Atacama Telescope (CCAT).

the thermal “bulge” largely cancels out gravitational sag. Note, from the right-hand column, that the effect of the panel mold errors is not dramatic at this observing frequency.

Figure 11 shows the same set of calculations, to simulate the beam pattern for the Mustang bolometric array receiver at 90 GHz. Now, in the bottom right-hand panel, with mold errors included and assuming a positive thermal gradient, the panel mold errors become relatively prominent. However, most observing at 90 GHz is done during nighttime hours and clear-sky conditions, when $\Delta T < 0$ would be expected.

Figures 12 and 13 show simulations at 45 and 115 GHz, respectively, using the 14-dB edge taper which is characteristic of the the standard GBT receiver horns.

7. Comparison with Observations.

7.1. Beam Maps. The prime motivation for this study was the observation that as the GBT primary surface improved with each iteration of holography mapping and actuator zero-point readjustment, the beam maps appeared to be converging to a distinct pattern, as shown by the sequence of images in Figure 14. The two most dominant features in the sidelobe pattern of the September 2009 map (the final image in the sequence) are the partial arcs, which are seen at elevation offsets around $\pm 40'$ in these 11.7 GHz holography beam maps. Corresponding features are evident in the model beam maps shown in Figure 3 (the gravitational error beam), Figure 7 (the thermal error beam), and Figure 10 (gravity and thermal, combined, error beam). There is a third prominent feature—the vertically aligned artifact which appears at negative elevation offsets near the bottom, center, region in each panel of Figure 14. We do not understand the origin of this feature; it does not appear in our model beams, and we believe it may be due to a spurious reflection in the telescope optics. Lunar scans taken at Q-band (43 GHz) at three different epochs of surface improvement are shown in Figure 15. In the elevation scans of the moon (shown in the lower panel of Fig. 15) the persistent “step” feature that is apparent corresponds to the partial-arc artifacts in the holography beam scans.

One can understand the origin of the two partial-arc artifacts as follows: Wavefront phase errors along a central swath of the primary mirror (i.e., aligned with the line of symmetry, from vertex to far edge of the dish) comprise a quasi-periodic phase grating, leading to grating lobes in the elevation direction. The arc length of each panel in the radial direction is 2.542 m, and in (x, y)-projection onto the aperture plane the length L of each panel is around 2.5 m, the actual lengths varying from $L_1 = 2.540$ m in Tier 1 to $L_{44} = 1.925$ m at Tier 44. Thus at a given wavelength, λ, the grating lobes in the elevation direction ought to be concentrated within the angular ranges $[-\lambda/L_{44}, -\lambda/L_1]$ and $[+\lambda/L_1, +\lambda/L_{44}]$. At 11.7 GHz the latter range corresponds to the zone between $34\farcm68$ and $45\farcm76$, indicated by the dotted lines in the top panel of Figure 16.

The panel mold error beam map (Fig. 9, bottom) has multiple partial-arc artifacts of the same nature as the two discussed above; in particular, the peak levels in these arcs all occur at zero cross-elevation offset. However, the pattern of quasi-periodicity in the central swath of the panel mold surface error map is rather complex, so the actual spacing of the artifact bands is not so readily explainable.

To investigate the relative importance of panel-scale gravitational and thermal gradient effects we have made detailed comparisons of four sets of holography data—two nighttime data sets:

(1) the Sept. 11, 2009 data set, acquired under very good conditions (i.e., low wind, late night, relatively stable air temperature);

(2) the Jan. 21, 2010 data set, acquired under prime nighttime conditions, characterized by unusually steady air temperature and excellent phase stability;

and two daytime data sets:

(3) the Nov. 21, 2009 data set acquired during during mid- to late morning, under sunny conditions; and

(4) a data set acquired on May 27, 2010 under similar conditions, but beginning at dawn.

We have only limited data on thermal conditions: air temperature from GBT Weather Station No. 2, and temperature measurements from areas near surface nodes 16+000 (for all 4 data sets) and 36+000 (for Sept. 11 and May 27, only). Mounted in the vicinity of each of these two nodes are a temperature sensor on the underside of a panel skin, and another attached to a nearby area of the back-up structure (BUS) (except that on May 4, 2010, one of the sensors at 36+000 was moved from the BUS beam to a panel Z-section rib).

Figure 16 shows the Sept. 11, 2009, holography beam map together with the Jan. 21, 2010, map. The mean measured thermal gradients are $\overline{\Delta T} = -2.69\,^{\circ}\mathrm{C}$ at 36+000 and $\overline{\Delta T} = -3.21\,^{\circ}\mathrm{C}$ at 16+000 for the Sept. 11 map (top panel); and a much smaller (in magnitude) thermal gradient, $\overline{\Delta T} = -0.45\,^{\circ}\mathrm{C}$ at 16+000, for the Jan. 21 map (lower panel). The two partial-arc artifacts appear significantly diminished in the Jan. 21 map, suggesting that thermal gradients may be the dominant effect.

Figure 17 shows the equivalent display for the Sept. 11 map and the Nov. 21 daytime map. For the latter, the observed mean thermal gradient at hoop 16+000 was $\overline{\Delta T} = +5.00\,^{\circ}\mathrm{C}$. The daytime holography data were acquired between 08:30 and 12:30, local time. In the daytime map, note the near disappearance of the partial arc features. Thus it appears that the positive thermal gradients characteristic of daytime, sunny conditions, may sometimes act to largely cancel out the gravitational distortion at 44° elevation, and at other mid-range elevation angles.

7.2. Surface Maps. The aperture-plane amplitude illumination and surface-error distributions are recovered from the beam maps via the usual Fourier inversion technique. However, because the main holography receiver is mounted at the Gregorian focus, rather than at prime focus, the outer radii of the derived surface error maps are contaminated with ring-like artifacts due to diffraction at the 8-m diameter subreflector. We filter out these artifacts by (1) removing the large-scale error, as given by a Zernike polynomial fit; (2) manually tabulating the positions of points along the observed diffraction rings; (3) fitting for low-order polynomials modeling the x-y positions of the ring centers, as a function of radial distance from the center of the aperture plane; (4) then at each location in the map, finding the median residual surface error along the best-fit circumferential diffraction ring arc (of angular size, say, 45°); and finally, (5) subtracting out these errors (and optionally adding the Zernike fit back into the surface error map). Here, the medium- and large-scale surface errors have been filtered out by subtraction of a 55-term Zernike polynomial model, and we do not add the Zernike model back in.

To facilitate comparison of the observed holography data with the gravity, thermal, and panel mold error models, we developed software to generate estimates of the tier-averaged panel error distributions from the surface-error maps. The raw average estimates were found to be overly sensitive to "outliers" (due, e.g., to malfunctioning actuators or to dish-edge artifacts), so we chose to use median and trimmed-average panel profiles. Figure 18 shows the trimmed-average profiles for the Sept. 11, 2009, data set (here the data have been trimmed, pointwise, at $\pm 2\sigma$). Observe that all panel tier-average profiles in the range from Tier 3 to Tier 44 show a prominent central depression and that the average profiles appear more to resemble the patterns of thermal deformation (shown in Fig. 6) than the patterns of gravitational sag (Fig. 2).

The tier-average panel profiles for all four dates are shown in the separate columns of Figure 19. The columns are arranged, left to right, in ascending order of mean temperature gradient $\overline{\Delta T}$ measured at node 16+000. The 42 rows in this display correspond to panel Tiers 3–44. (The Tier 1 and 2 mean profiles are ill-behaved, because of low S/N due to edge effects, and ice damage to a few panels.) Within each row, a common vertical scale is used for all four plots.

The leftmost column of Figure 19 is a redisplay of the Sept. 11, 2009 mean profiles (already shown in Figure 18), for which $\overline{\Delta T} = -2.69\,^{\circ}\mathrm{C}$ at node 16+000. The second column shows the Jan. 21, 2010 data ($\overline{\Delta T} = -0.45\,^{\circ}\mathrm{C}$); the third, the May 27, 2010 data ($\overline{\Delta T} = +2.53\,^{\circ}\mathrm{C}$); and the fourth column, the Nov. 21, 2009 data ($\overline{\Delta T} = +5.00\,^{\circ}\mathrm{C}$). The predominant trend, left to right, is from a typically concave, or cup-shaped profile to a flattish, or even slightly bulged profile.

The tier-average panel r.m.s.'s for each of the four dates are shown in Figure 20, via a simple line plot—as well as a 3-D bar chart. The overall area-weighted surface (systematic deformation) r.m.s. at 44° elevation can be computed as

$$\sigma_{\mathrm{aperture}} = \sqrt{\frac{\sum_{k=1}^{44} N_k A_k \sigma_k^2}{\sum_{k=1}^{44} N_k A_k}}\,, \tag{1}$$

where N_k denotes the number of panels in the k^{th} tier, A_k the area of the panel (in aperture-plane projection), and σ_k the tier-average r.m.s. For the four dates of interest, the $\sigma_{\rm aperture}$ values are $(80.4, 65.5, 54.1, 45.6)\,\mu$m respectively, with the dates ordered as in Figure 19. (Here, however, we have excluded Tiers 1, 2, and 44 from the two summations.)

8. Discussion. A main conclusion of our work is that thermal gradients are the major contributor of systematic deformations of the surface panels, predominating over gravitational error and panel mold error. This was anticipated by the telescope designers—we saw, for example, in Figure 4 that the 1992 FEMs predict panel thermal deformation exceeding the gravitational for $\Delta T = -2\,^\circ$C. On the subject of painting the surface panels, Dave Hogg in GBT Memo. No. 46 writes "Sebastian [von Hoerner] points out that the surface must be painted, since an unpainted surface illuminated by sunlight can rise to a temperature $40\,^\circ$C higher than ambient, whereas a painted surface will probably stay within $5\,^\circ$C of ambient. John [Payne] notes that the paint is a mixed blessing, since it radiates so effectively in the infrared. Thus at night that the surface can develop a temperature difference of $5\,^\circ$C between the front and the back." von Hoerner, in his 1971 report on thermal and wind deformations of the surface panels designed for the proposed 65-m telescope [**7**, §I.3], comments that "the white paint improves the thermal deformations by a factor 5.3 during sunshine, but makes them worse by 40% during clear nights."

For thermal monitoring of the GBT structure, the PTCS group uses of order two dozen precision temperature sensors, mounted at various locations on the alidade, the feedarm, the BUS, and on two surface panels [**11**]. Paired thermal sensors are mounted on the backside of the panel skin and on an adjacent BUS member, at a panel near the center of Tier 16 and on another near the center of Tier 36. Data from these sensors were recorded nearly continuously from Oct. 1, 2008, through Sept. 30 of the following year. Figure 21 shows histograms of the 10-minute median temperature differences observed during the four-hour nighttime period, midnight to 4AM EST, and during the daytime period 11AM–3PM, over the span of that entire year. The quartile values of the inferred temperature gradients are at node 16+000, $(-2.68, -1.44, -0.62)\,^\circ$C (nighttime) and $(0.67, 2.36, 4.60)\,^\circ$C (daytime); and at node 36+000, $(-3.22, -1.65, -0.73)\,^\circ$C (nighttime) and $(0.68, 2.43, 4.61)\,^\circ$C (daytime). Note the apparent bimodality of the nighttime ΔT distributions. The left-hand peak likely corresponds to predominantly clear-sky conditions, and the right-hand one to overcast (unfortunately, we do not have quantitative data on meteorological conditions such as cloud cover and precipitation). The implication for high-frequency (e.g., 3-mm) observing is that, when atmospheric transparency is at its best, the surface efficiency is likely sub-optimal.

Figure 22 shows the temperature gradients measured during the Sept. 11, Nov. 21, Jan. 21, and May 27 holography runs. The ΔT curves of Sept. 11 are likely fairly representative of nighttime, non-overcast conditions; and those of Nov. 21, typical of non-overcast daytime conditions. The Jan. 21 data, with very small gradients, correspond to about the eighty-fifth percentile in the nighttime distribution curve (solid blue) of Figure 21.

For all holography runs prior to that of May 27, 2010, the only primary surface temperature gradient data that we have available are measurements ΔT defined by $T_{\rm skin} - T_{\rm BUS}$ rather than $T_{\rm skin} - T_{\rm rib}$, at surface nodes 16+000 and 36+000. For proper comparison with the thermal gradient model, described in §3, one should use $T_{\rm skin} - T_{\rm rib}$. For the May 27 daytime run, however, we do have $T_{\rm skin} - T_{\rm rib}$ measurements from node 36+000 as well as $T_{\rm skin} - T_{\rm BUS}$ measurements from node 16+000, which are shown by the purple and orange curves in Figure 22. During the mid-morning hours (~9AM–10AM) we see a mean ratio $\dfrac{(T_{\rm skin} - T_{\rm BUS})_{16+000}}{(T_{\rm skin} - T_{\rm rib})_{36+000}} \approx 6$ (unfortunately, we do not have simultaneous measurements of $T_{\rm skin}$, $T_{\rm rib}$, and $T_{\rm BUS}$ at either 16+000 or 36+000). Now, we do have archival data from the thermal sensors, including $T_{\rm skin}$ and $T_{\rm rib}$ measurements at node 36+000 from May 5, 2010 to present. If we compare the May–September data of 2010 with archival data from May–September 2008 and 2009, we find (see Appendix for details) a mean diurnal ΔT ratio—16+000 (skin minus BUS) over 36+000 (skin minus rib)—of ~3.0 during the dark of night (4AM or 5AM EST), and ~5.0 during mid-morning (say, 10AM). This is relevant to Figure 23, described below.

Based on our comment in §7 that a positive thermal gradient might act to largely cancel out the panel-scale gravitational deformation, one might ask "for a given elevation angle of the telescope, what particular ΔT most nearly achieves full cancellation?" Let $A_{\rm grav}({\rm elev})$ represent the FEM gravitational error pattern (as in the left-hand column of Fig. 3) and $A_{\rm therm(-2C)}$ the FEM thermal pattern (Fig. 7, top), each evaluated over a suitably fine discrete sampling grid in the aperture-plane. We find that numerical minimization of the expression

$$\sigma = \left\| A_{\mathrm{grav}}(44^\circ) - \frac{a}{2} A_{\mathrm{therm}(-2\mathrm{C})} + b \right\|_2 , \tag{2}$$

yields the solution $a = 1.997\,^\circ\mathrm{C}$, $b = -68.5\,\mu\mathrm{m}$, at the minimum $\sigma_{\mathrm{opt}} = 20.9\,\mu\mathrm{m}$ ($\|\cdot\|_2$ denotes Euclidean L_2 norm). Thus, at elevation 44°, with panel thermal gradients of about $2\,^\circ\mathrm{C}$, we find that the gravitational and thermal errors should nearly cancel (all but about $21\,\mu\mathrm{m}$ r.m.s.). They would do so more or less equally well, depending on the particular location of a panel on the curved surface. The net effect is shown in Figure 23. In this calculation we have assumed $75\,\mu\mathrm{m}$ r.m.s. panel manufacturing error, $50\,\mu\mathrm{m}$ r.m.s. panel setting error, and $70\,\mu\mathrm{m}$ r.m.s. subreflector surface error. The colored points in this figure show the fit to holographic estimates of the total effective surface error on small spatial scales. These dots represent the median absolute deviation (MAD) about the median residual in the holography map, scaled by a factor 1.48. (For normally distributed data, the standard deviation is a factor $\sim$1.48 times larger than the expectation of the MAD estimator.) Note that the measured thermal gradients shown in Figure 23 have been scaled by a factor k, where k is the reciprocal of the ratio defined in the preceding paragraph.

The location of the orange and blue points above the predicted curve for the total small-scale error may be due to the inability of our measurement method to remove the effect of the (undoubtedly) time-variable medium-scale error distribution during these four-hour daytime holography maps. In any case, the colored rectangles represent the $\sigma_{\mathrm{aperture}}$ values computed via Equation 1. The consistent downward trend in $\sigma_{\mathrm{aperture}}$ vs. ΔT is in reasonable agreement with the thermal model prediction. Thus, we conclude that the aggregate contribution to total surface r.m.s. from individual panel deformation ranges from 40 to 100 microns depending on environmental conditions. This result suggests that a further improvement to the high frequency efficiency of the GBT in clear nighttime skies could be achieved if the panel temperature gradient could be reduced by some means of active compensation.

Earlier figures, in the present memorandum, showing holography beam maps and model beam patterns did not include plot legends, to show the intensity transfer function which had been used in the display. In fact, identical transfer functions were used for all the model beam maps, as well as for the holography beam maps. Figure 24 is a re-display of two of these images, together with appropriate plot legends.

References

[**1**] Radiation Systems, Inc., *NRAO Green Bank Telescope Reflector Panels, Design and Analysis*, RSi Technical Memo. No. 101, Sterling, VA, December 1992.

[**2**] Korbeeck, J., Bennink, E., Jansen, A., Koppert, M., Lahaije, R., Plantenga, T, Janssen, B., and ter Harr Romeny, B. M, "Warping a neuro-anatomy atlas on 3D MRI data with radial basis functions", in *8th International Mathematica Symposium*, Avignon, June 2006.

[**3**] Greve, A. and Bremer, M., *Thermal Design and Thermal Behaviour of Radio Telescopes and Their Enclosures*, Springer-Verlag, Heidelberg, 2010.

[**4**] Hogg, D., "Painting the surface of the Green Bank Telescope", GBT Memo. No. 46, National Radio Astronomy Observatory, Green Bank, WV, March 22, 1990.

[**5**] Norrod, R. D., "Test report on solar diffusion of painted reflectors", GBT Memo. No. 128, National Radio Astronomy Observatory, Green Bank, WV, April 26, 1995.

[**6**] von Hoerner, S., "Thermal and wind deformations of the surface plates", 65-Meter Report No. 36, National Radio Astronomy Observatory, Green Bank, WV, January 20, 1971.

[**7**] von Hoerner, S., Memorandandum to W. G. Horne and the 25-m group, 25-Meter Millimeter Wave Telescope Memo. No. 36, National Radio Astronomy Observatory, Green Bank, WV, February 23, 1981.

[**8**] Schwab, F. R., "Economization in number of surface panel molds", GBT Memo. No. 35, National Radio Astronomy Observatory, Green Bank, WV, February 15, 1990.

[**9**] Schwab, F. R., "Distortions of the antenna pattern due to surface-panel imperfections", GBT Memo. No. 44, National Radio Astronomy Observatory, Green Bank, WV, March 18, 1990.

[**10**] MacDonald, D. R., Woody, D. P., Bradford, C. M., Chamberlin, R., Dragovan, M. W., Radford, S. J. E., Sebring, T. A., Zmuidzinias, J., and Goldsmith, P. F., "Cornell Caltech Atacama Telescope primary mirror surface sensing and controllability", in *Ground-Based and Airborne Telescopes II*, Stepp, L. M., and Gilmozzi, R., Eds., Proc. SPIE Vol. 7012, 2008.

[**11**] Ray, J., "Antenna temperature sensor installation plan", PTCS Project Note 7.1, National Radio Astronomy Observatory, Green Bank, WV, April 14, 2003.

Supplementary Material

An Appendix of supplementary material is available separately from this report; see

`https://safe.nrao.edu/wiki/pub/GB/Knowledge/GBTMemos/GBTMemo271.Appendix.pdf`.

Three additional figures are included: auto-scaled plots of the tier-average panel profiles for the other three data epochs besides Sept. 11, 2009 (which was already shown in Fig. 19). Also included is the transcript of a *Mathematica* run used for the analysis of the mean diurnal behavior of surface-panel thermal gradients.

Figure 1. *(Top)* A panel assembly is held against its tooling fixture as aluminum skins are epoxied to the rib structure. *(Middle)* Panels on the assembly line in the neighborhood of the paint shop; front panels have received only zinc chromate primer coat. Note the rib structure and edge stiffeners. *(Bottom)* Finished panels awaiting final inspection.

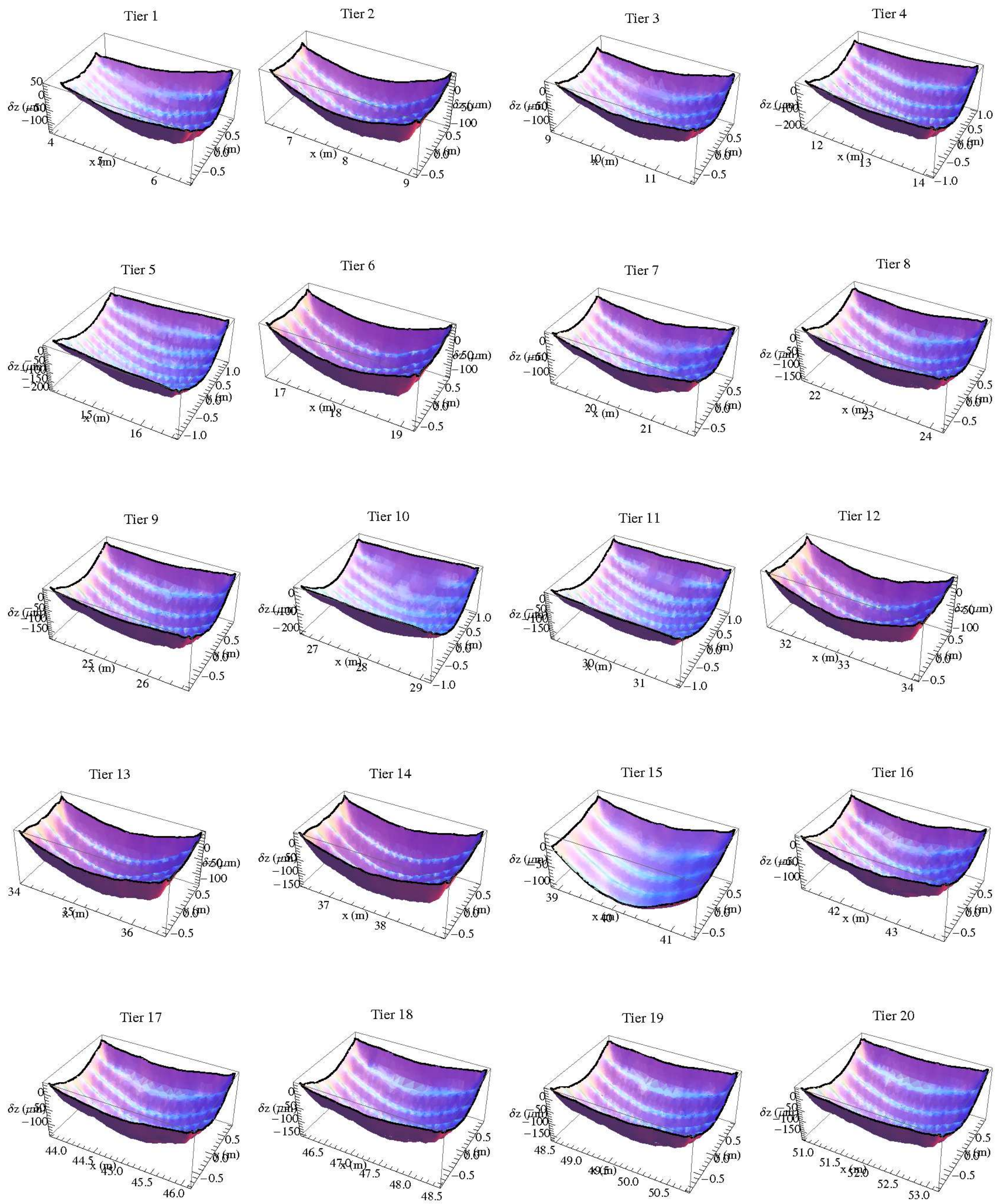

Figure 2. Finite-element models of GBT panel gravitational deflection, by tier, for panels supported horizontally. The interior ridge-like features appear at the positions of the inner radial ribs. The number of ribs may be five (as in the case of Tier 2), seven (as in Tiers 3 and 4), or nine (as in Tier 5). All panels are within 3.1 mils (79 μm) standard deviation, according to the FEM. These plots show the axial error δz (i.e., in the boresight direction), in microns, as a function of aperture-plane (x, y)-coordinates, here assuming the panel to be centered on the y-axis. The panel molds were not designed to compensate for any fraction of the typical expected gravitational sag. *(Continued on next page.)*

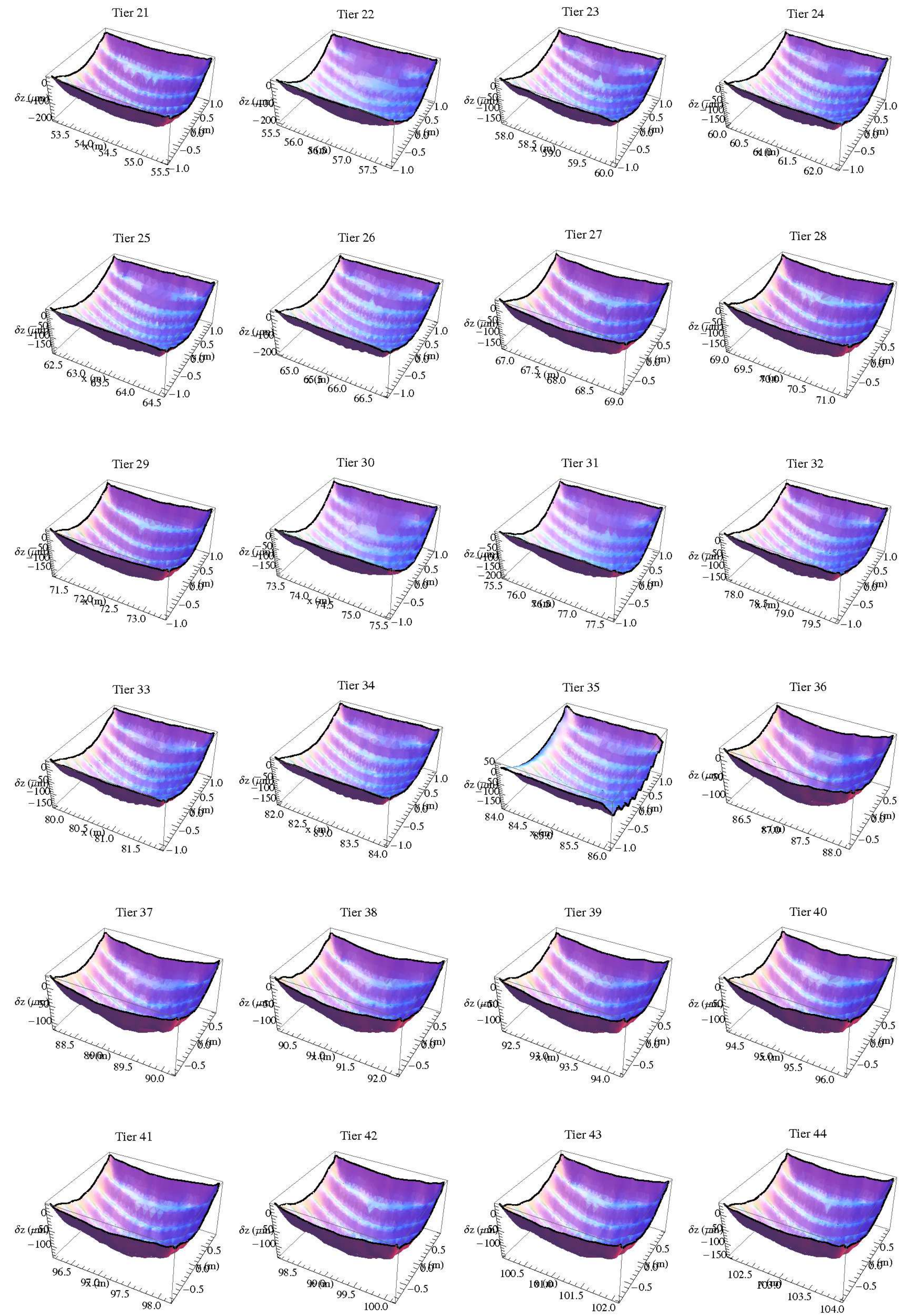

Figure 2 *(Continued)***.** Gravity models for Tiers 21–44.

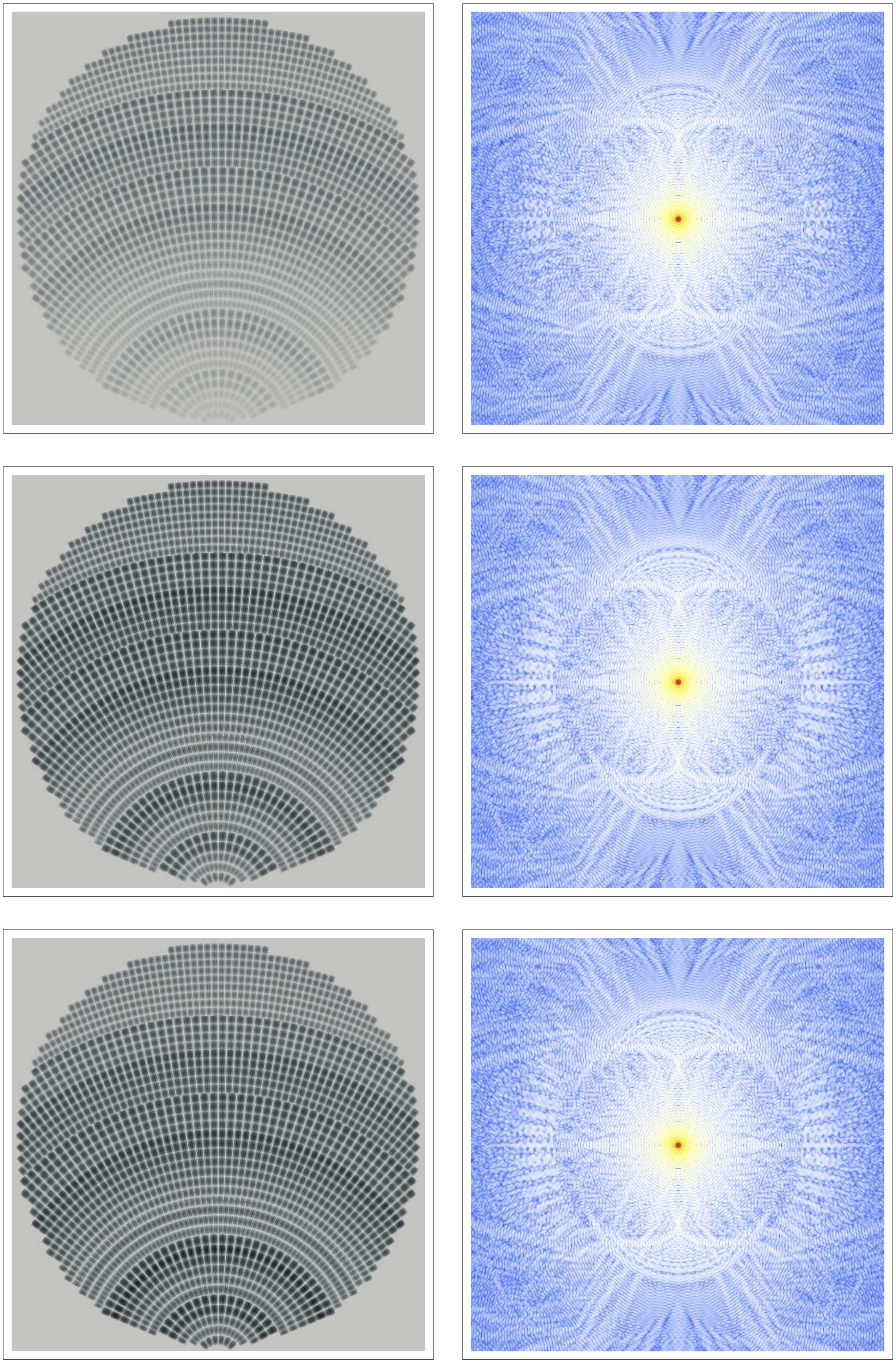

Figure 3. *(Left Column)* The gravitational component of the surface error distribution, as estimated by the finite-element modeling, for elevation angles of 5°, 44°, and 90° (top to bottom). Darker shades in this display correspond to deeper depressions. *(Right Column)* The corresponding beam patterns, calculated for an observing frequency of 11.7 GHz and a 10-dB edge taper. While the differences between the 5° and 44° beam patterns are fairly evident, those between 44° and 90° are hardly discernible in this display. The beam area shown here is $128' \times 128'$.

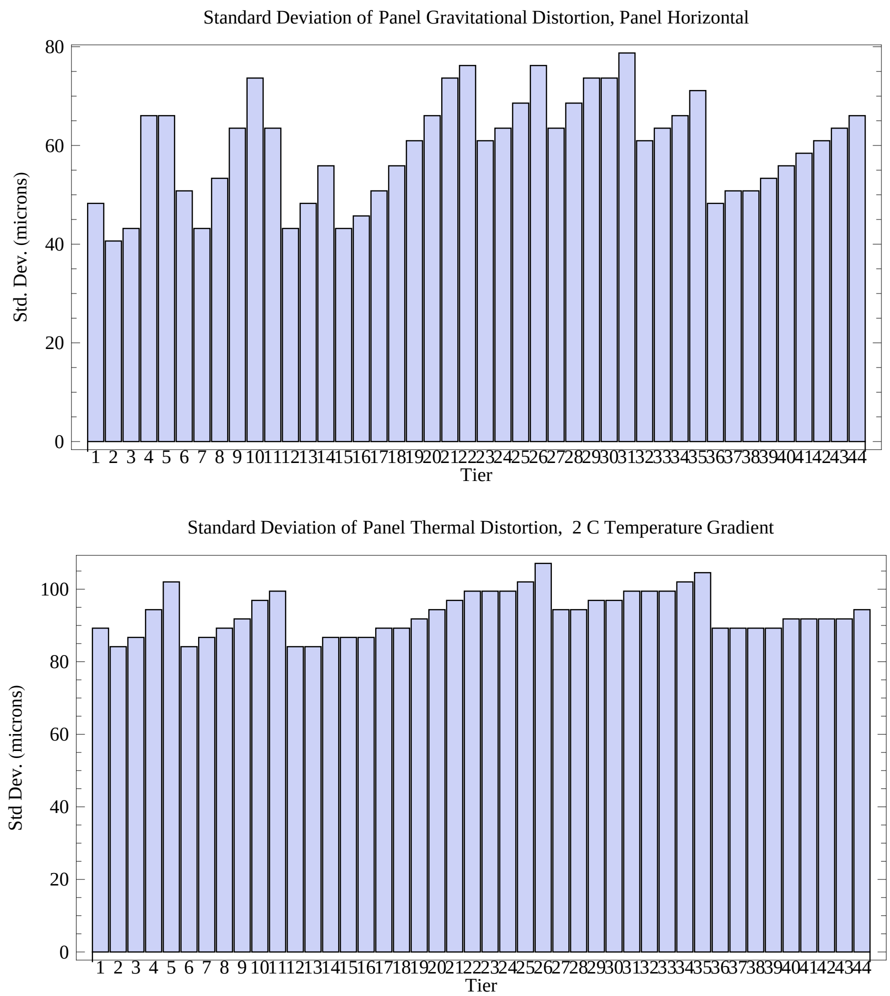

Figure 4. *(Top)* A plot of the standard deviation of the finite-element modeled gravitational distortion of the panels, by tier. All panels are modeled in a horizontal position, with the gravitational acceleration vector acting perpendicularly to the plane of the support points. *(Bottom)* Standard deviation of the FEM thermal distortion, assuming a front-to-back temperature gradient of 2 °C.

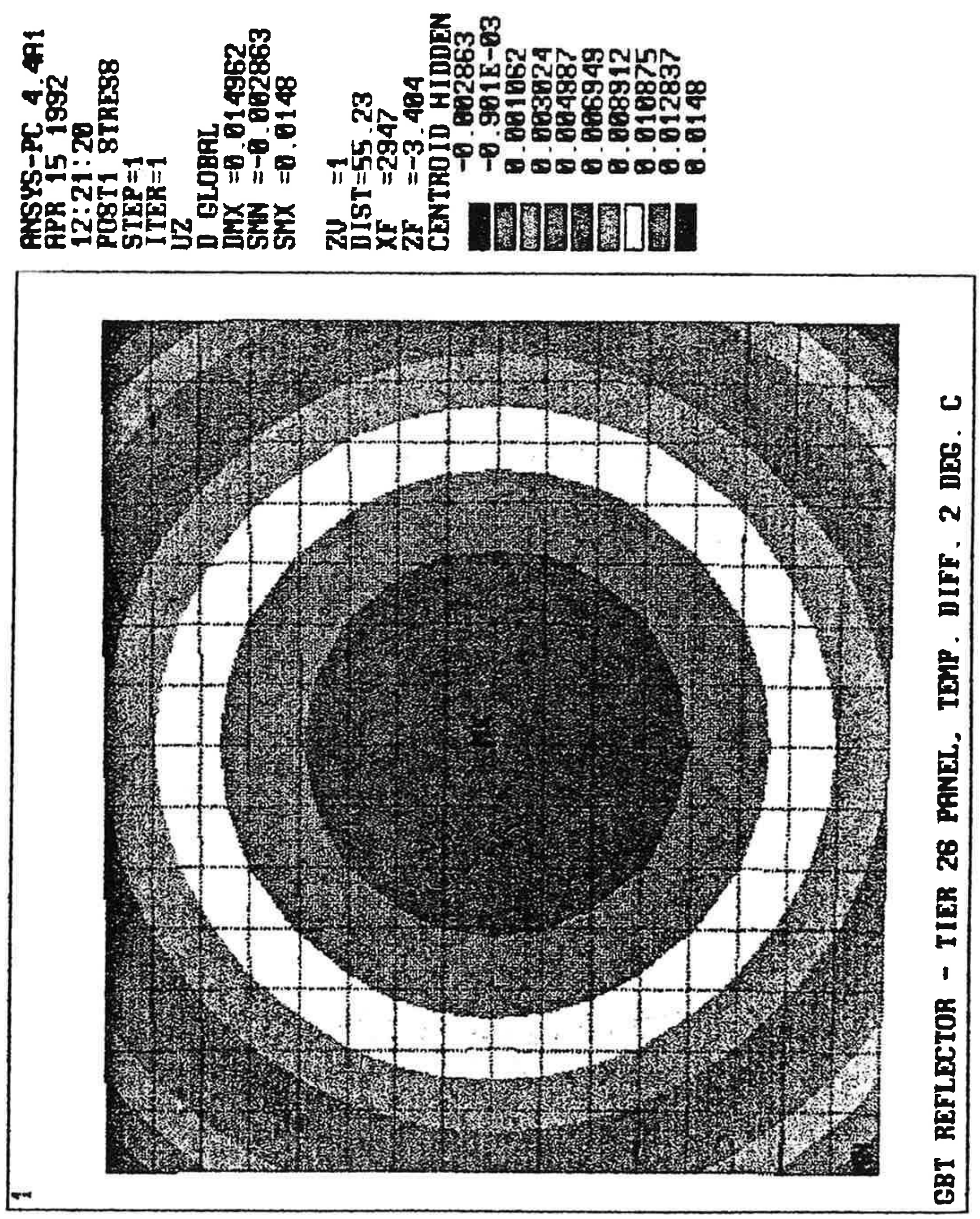

FIGURE 11.

Figure 5. Contour plot of thermal FEM for a Tier 26 panel, and a thermal gradient $\Delta T = 2\ °\mathrm{C}$. This is a reproduction of a figure from the contractor's report, [**1**].

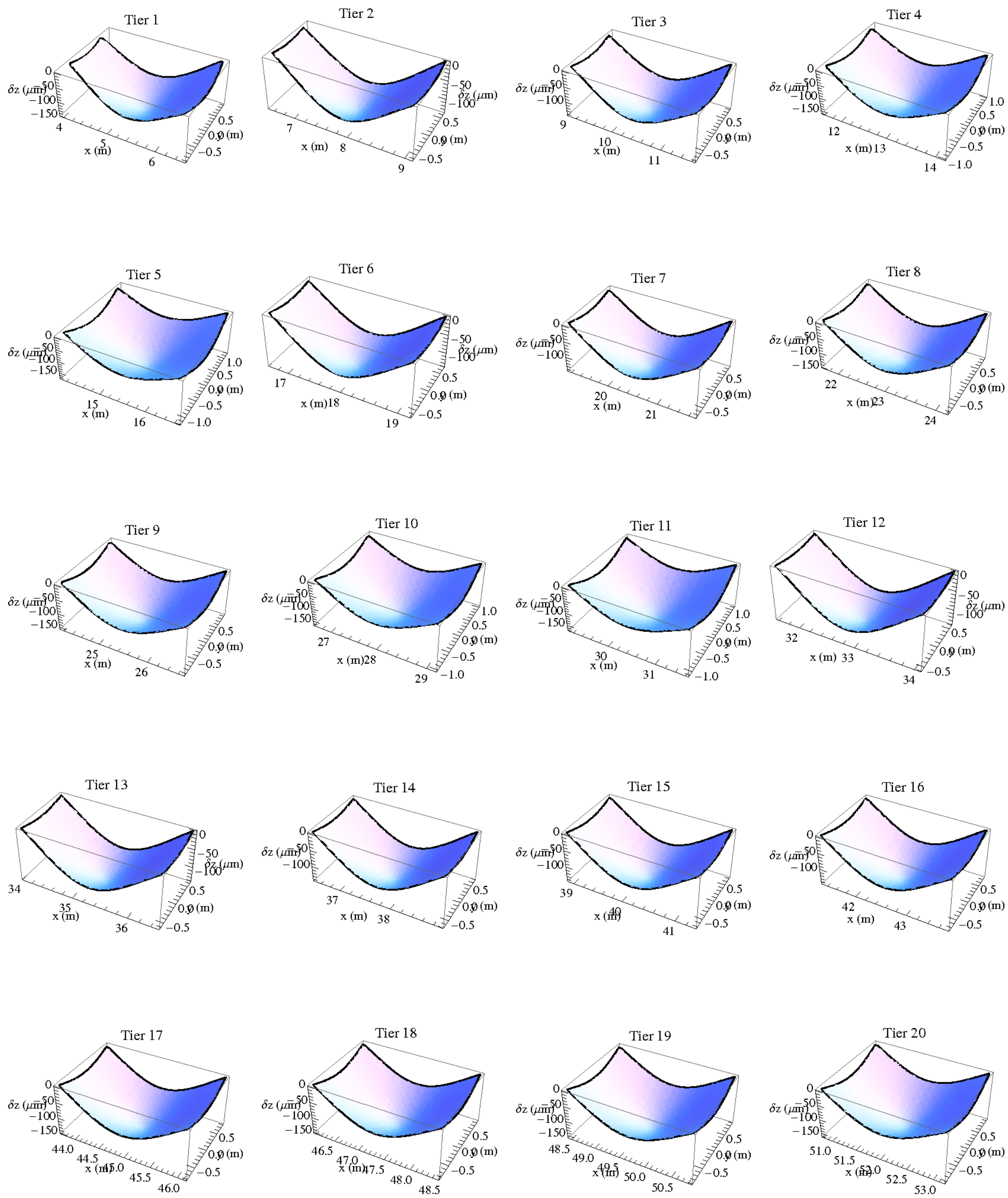

Figure 6. Finite-element models of GBT panel deformation due to a front-to-back thermal gradient $\Delta T = -2\,^{\circ}\mathrm{C}$. A negative ΔT in the range of $-1\,^{\circ}\mathrm{C}$ to $-2\,^{\circ}\mathrm{C}$ would be characteristic of benign nighttime observing conditions. For $\Delta T < 0$ the panel deformation Δz is negative, as with the gravitational distortion. A positive ΔT, as would be expected during daytime conditions, could act to cancel out the gravitational deformation. *(Continued on next page.)*

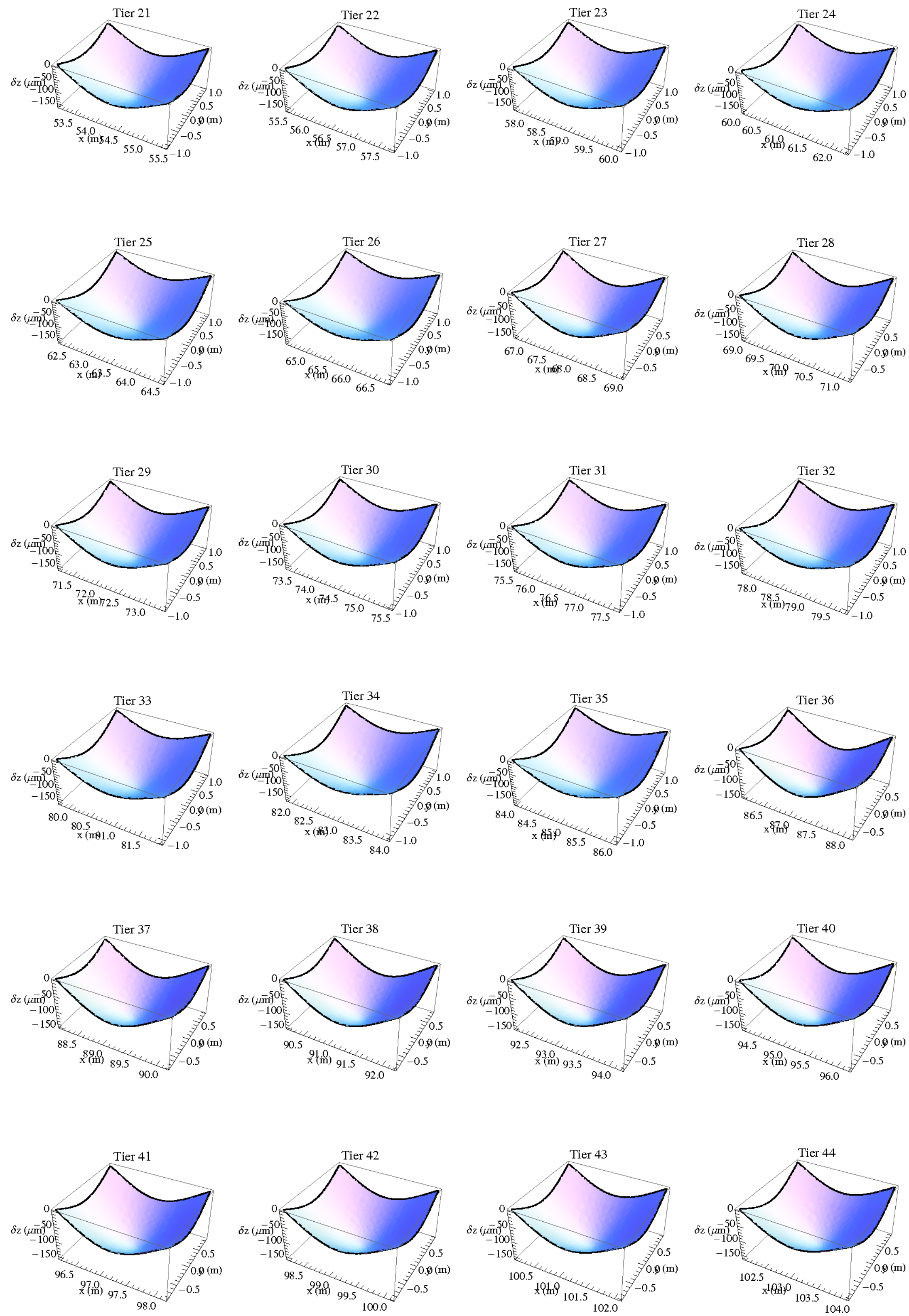

Figure 6 *(Continued)***.** Finite-element thermal gradient models for Tiers 21–44.

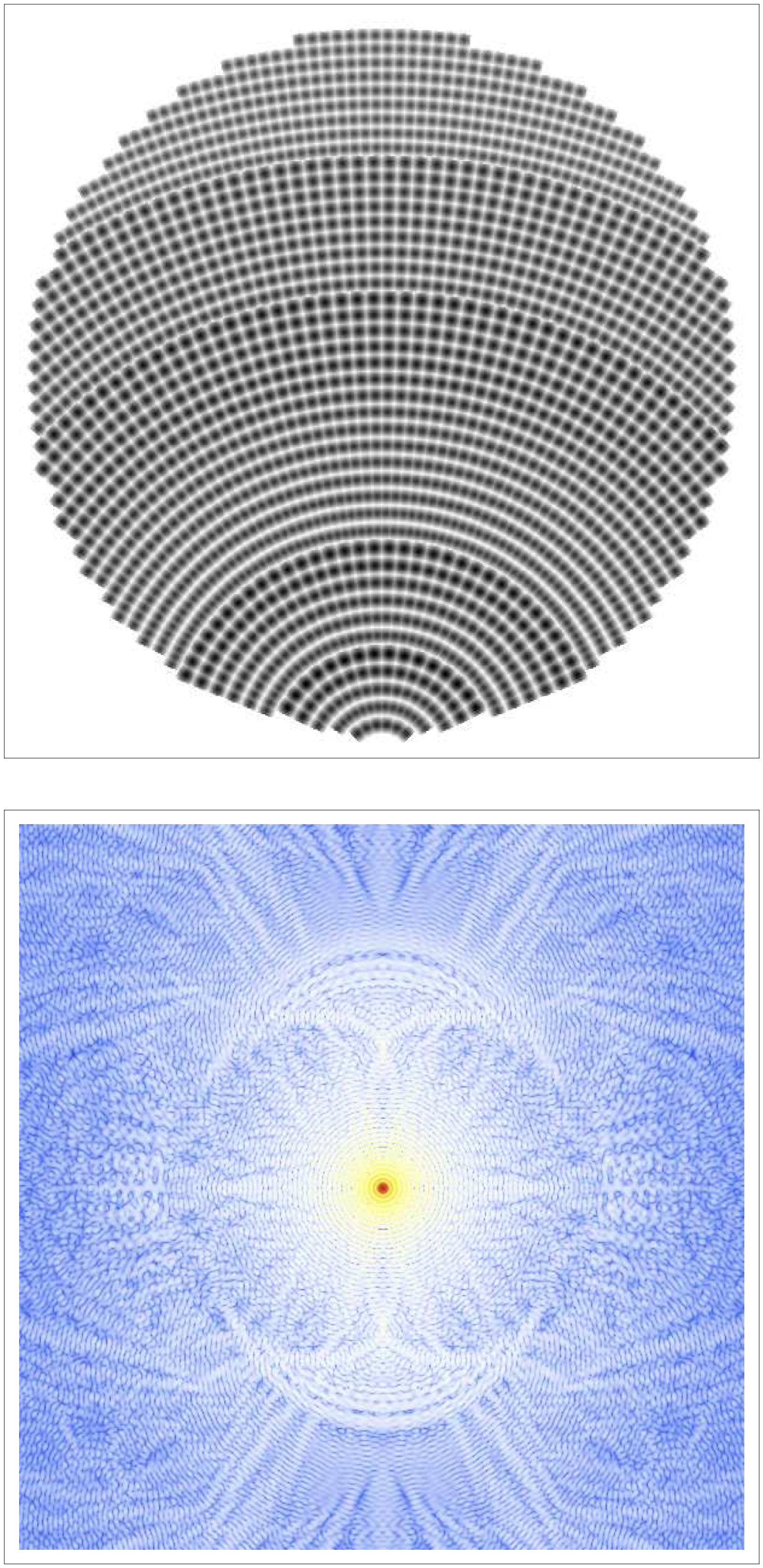

Figure 7. *(Top)* Finite-element model surface error distribution corresponding to a thermal gradient $\Delta T = -2\,^{\circ}\mathrm{C}$ through every panel. *(Bottom)* The corresponding simulated beam map at 11.7 GHz. Compare with the gravitational error patterns of Figure 3. The beam area shown here is $128' \times 128'$.

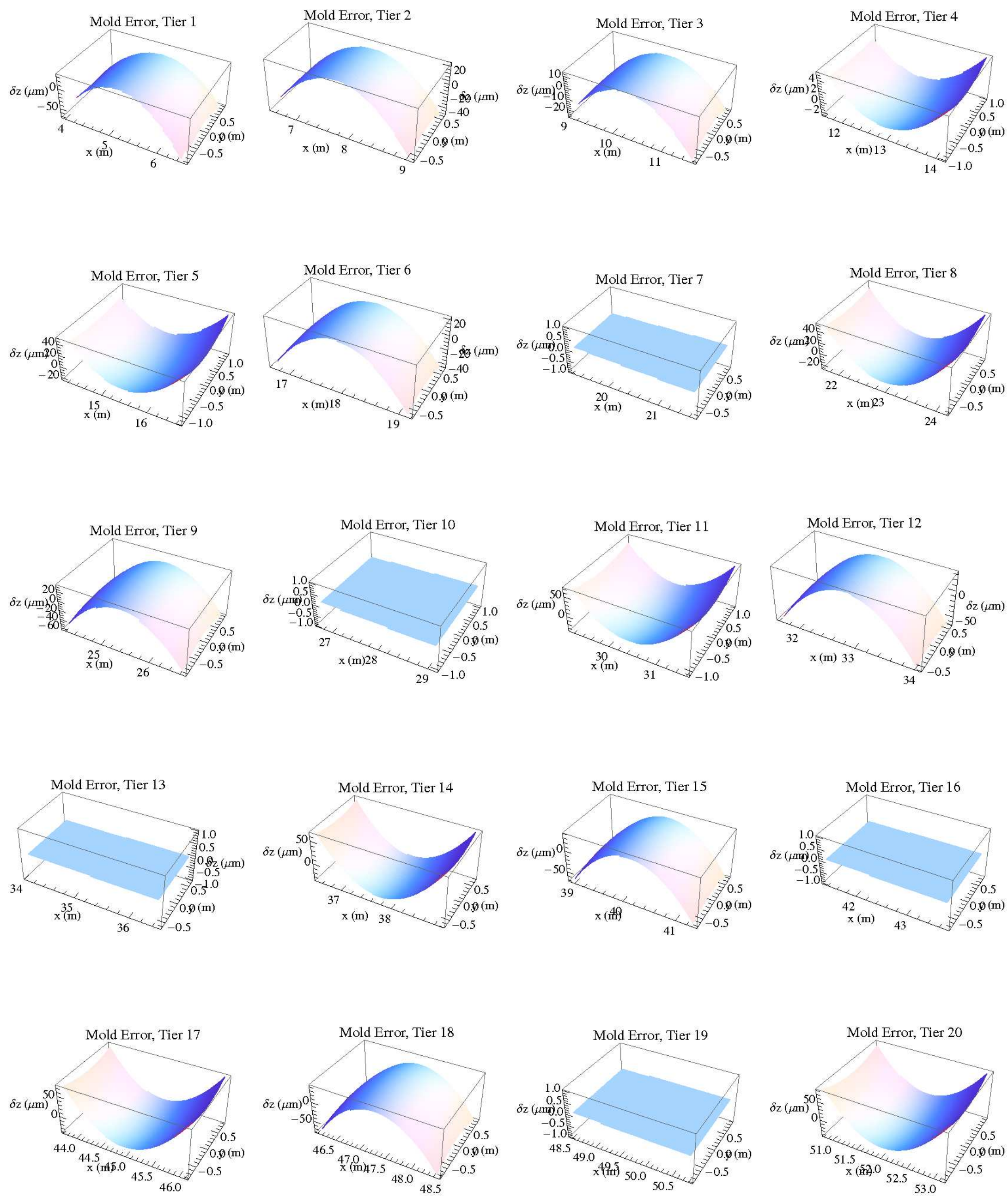

Figure 8. The designed-in panel mold error, which is a consequence of reducing the number of panel tooling fixtures from forty-four to sixteen, shown for each panel tier. *(Continued on next page.)*

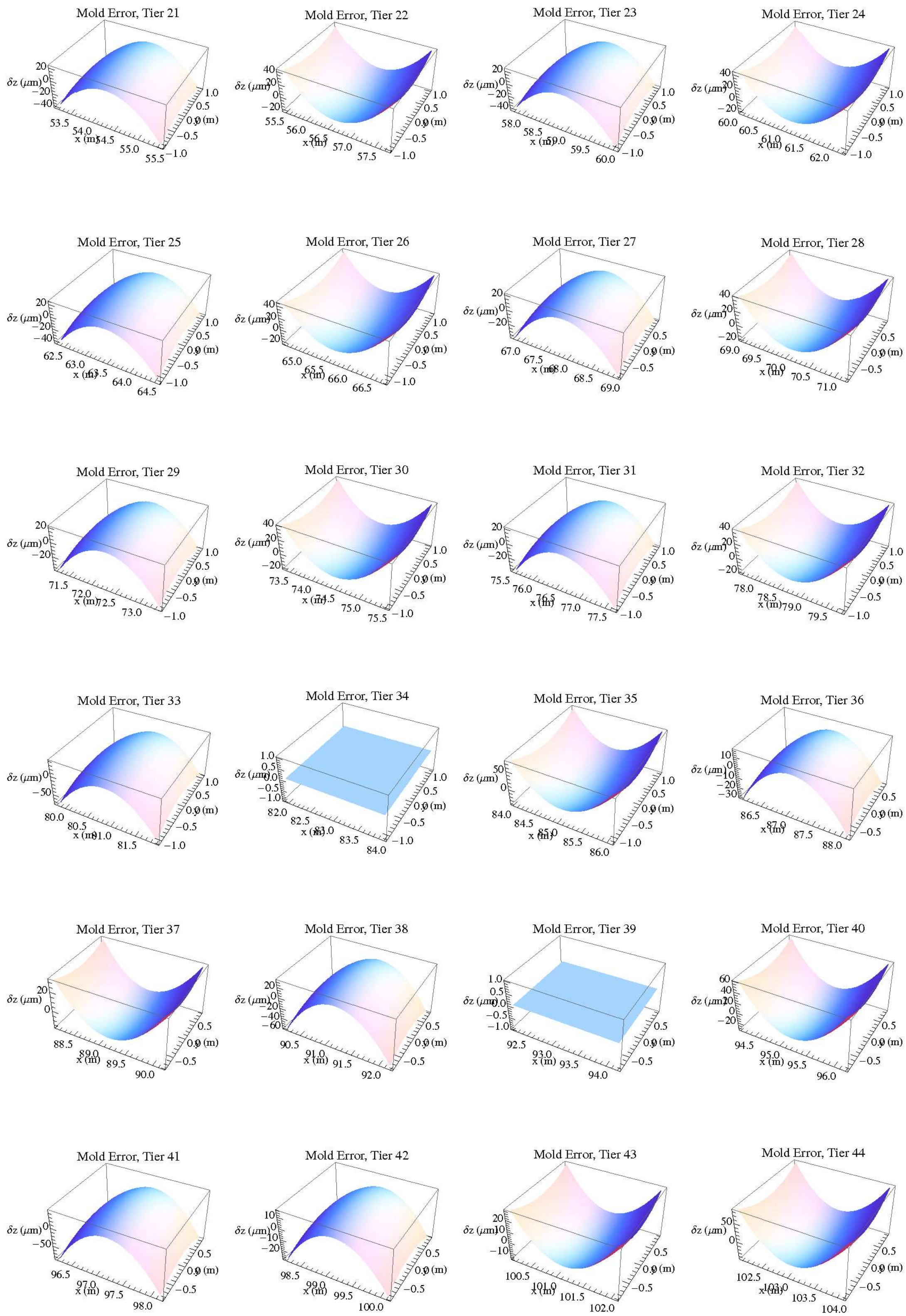

Figure 8 *(Continued)***.** Panel mold error plots for Tiers 21–44.

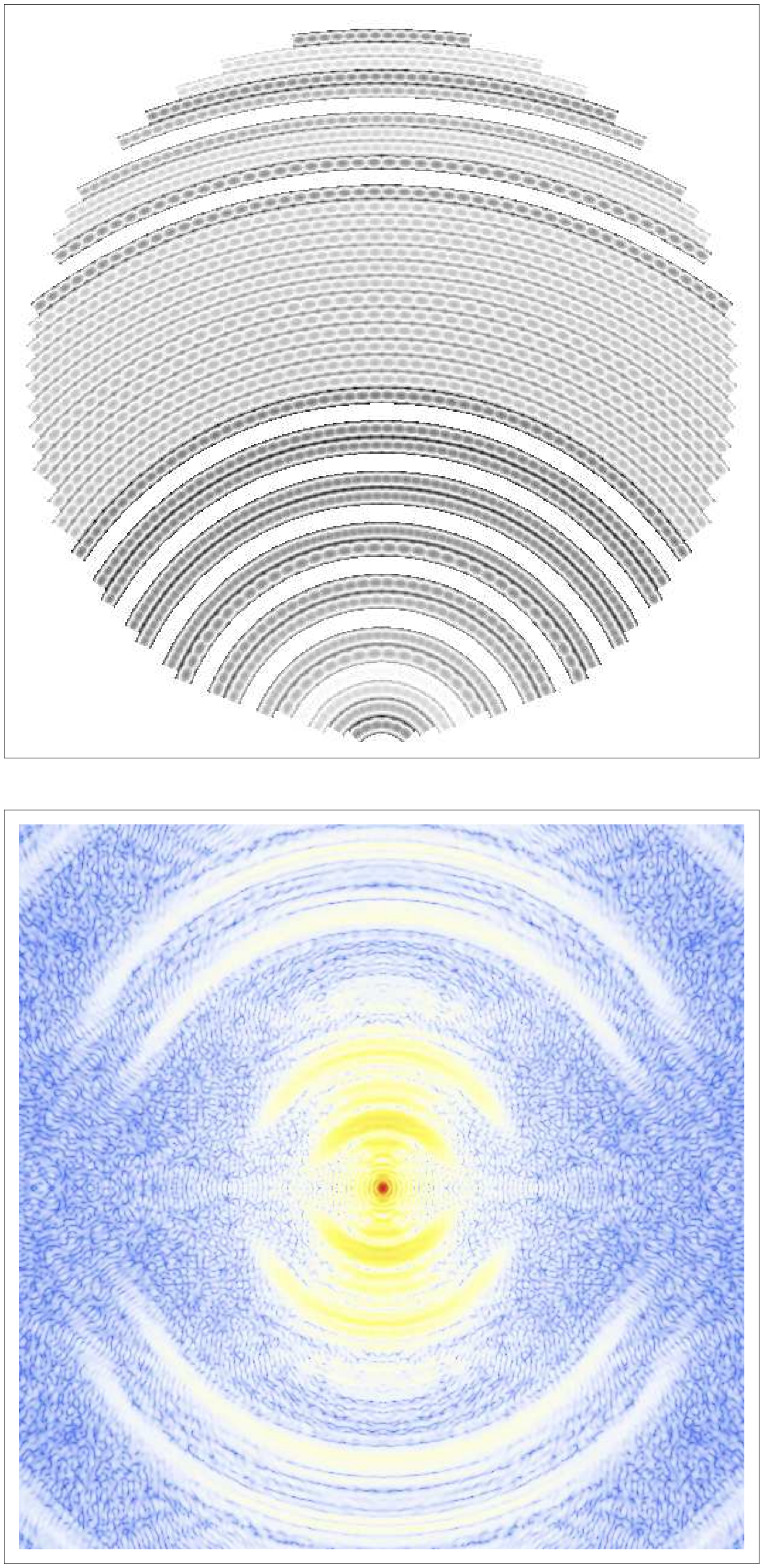

Figure 9. *(Top)* Panel mold surface error distribution. *(Bottom)* The corresponding theoretical beam map at 11.7 GHz, which looks quite horrendous. Compare with the gravitational (Fig. 3) and thermal (Fig. 7) error beam maps (which are displayed with the same transfer function as used here; Fig. 26 includes a color bar). Fortunately, the gravitational, thermal, panel-setting, and random surface errors greatly diminish the strong, near-in sidelobes of the panel mold error beam.

11.7 GHz Error Beam Maps (10-dB Edge Taper); Elevation 44°

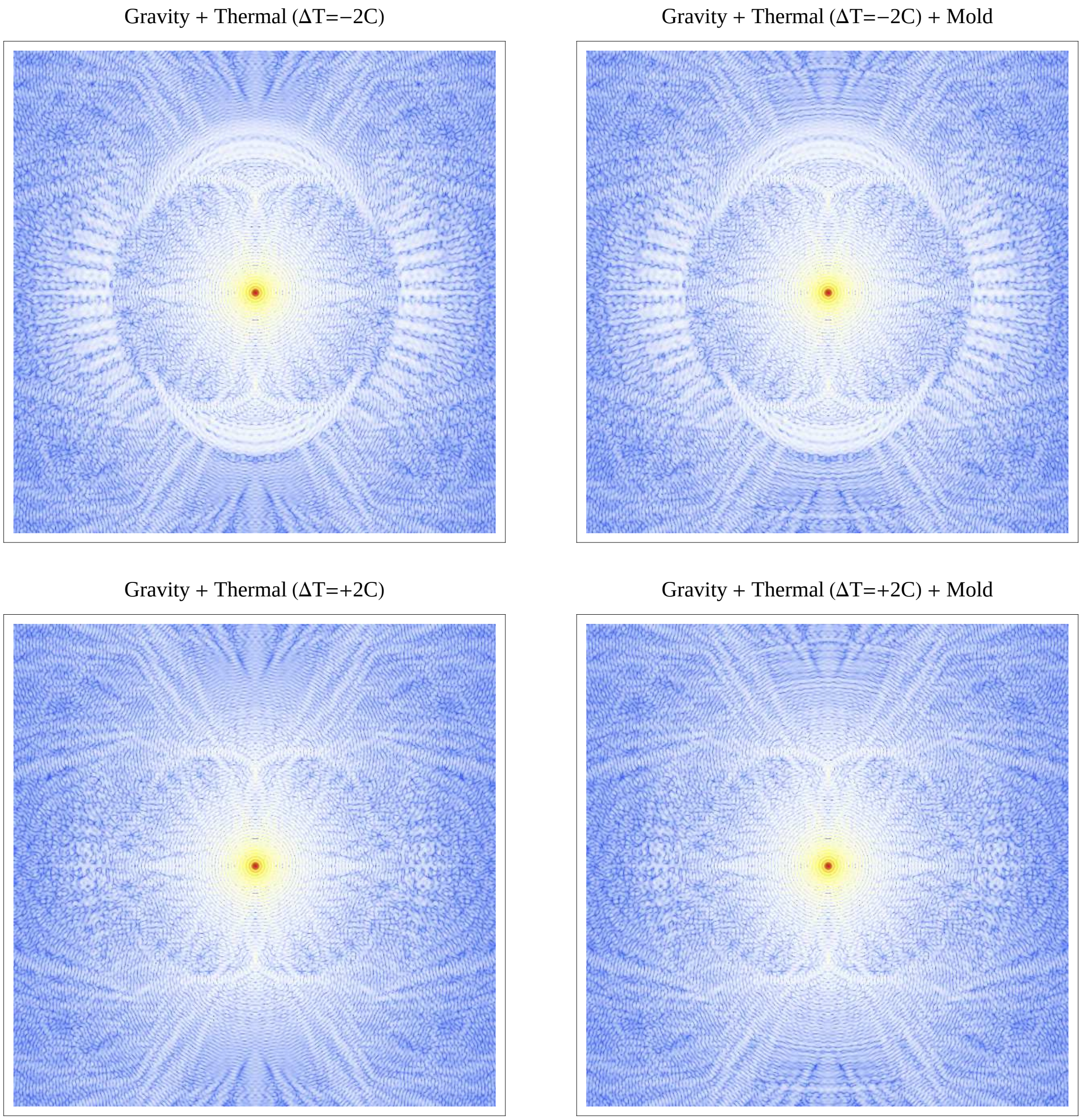

Figure 10. Simulations of the GBT beam pattern at 11.7 GHz (the frequency of the satellite beacon signals observed with the holography receivers). The left-hand column includes gravitational error, computed for 44° elevation, and thermal error corresponding to a thermal gradient $\Delta T = -2\,^{\circ}\mathrm{C}$ *(Top)* and $\Delta T = +2\,^{\circ}\mathrm{C}$ *(Bottom)*. The right-hand column includes designed-in panel mold error, in addition to the gravitational and thermal errors. The beam area shown here is $128' \times 128'$.

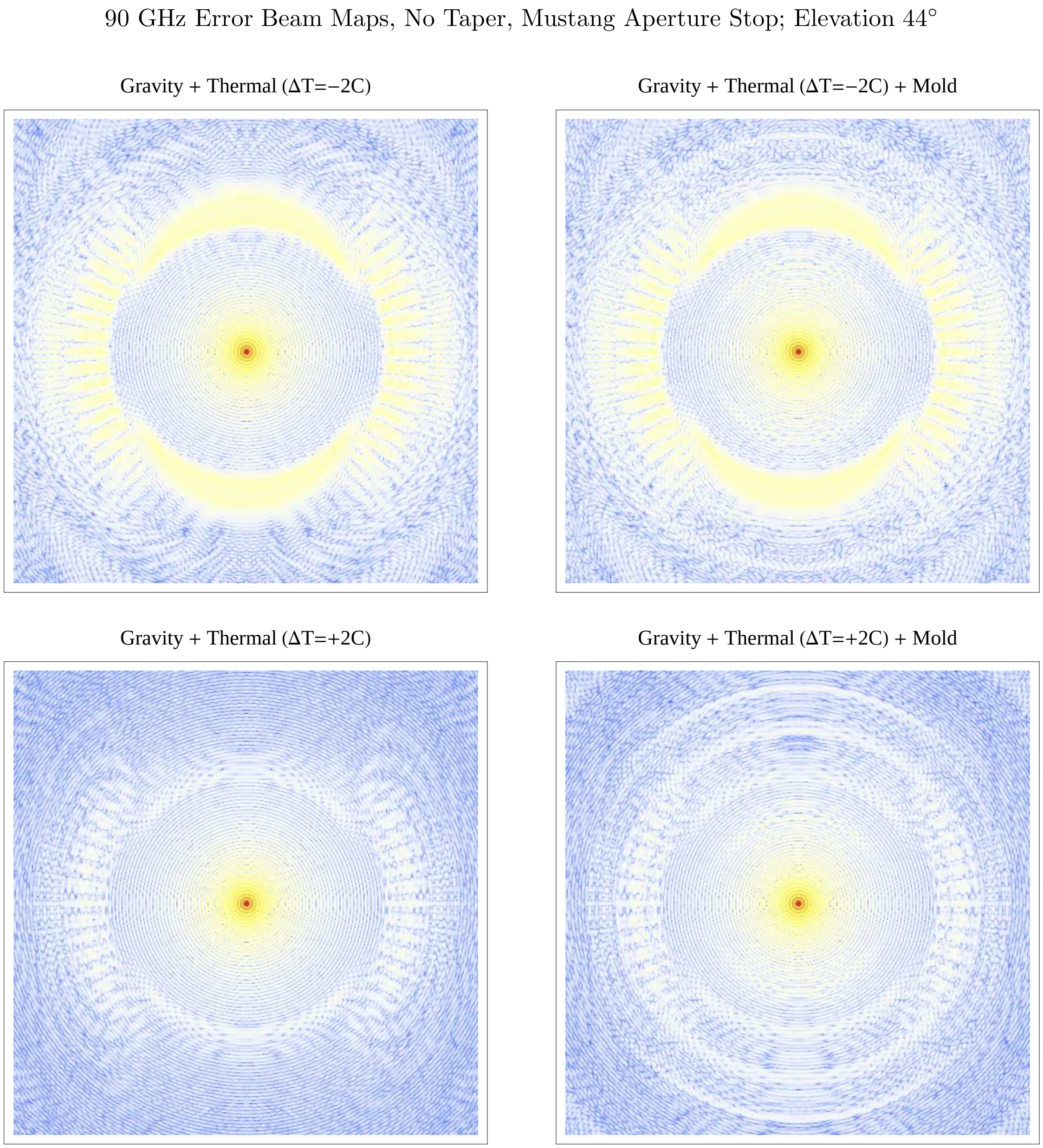

Figure 11. Simulations of the (monochromatic) GBT beam pattern at 90 GHz and 44° elevation, assuming a $D =$ 90-m aperture stop as used by the Mustang bolometer array receiver. The beam area shown here is (approximately) $17' \times 17'$.

45 GHz Error Beam Maps (14-dB Edge Taper); Elevation 44°

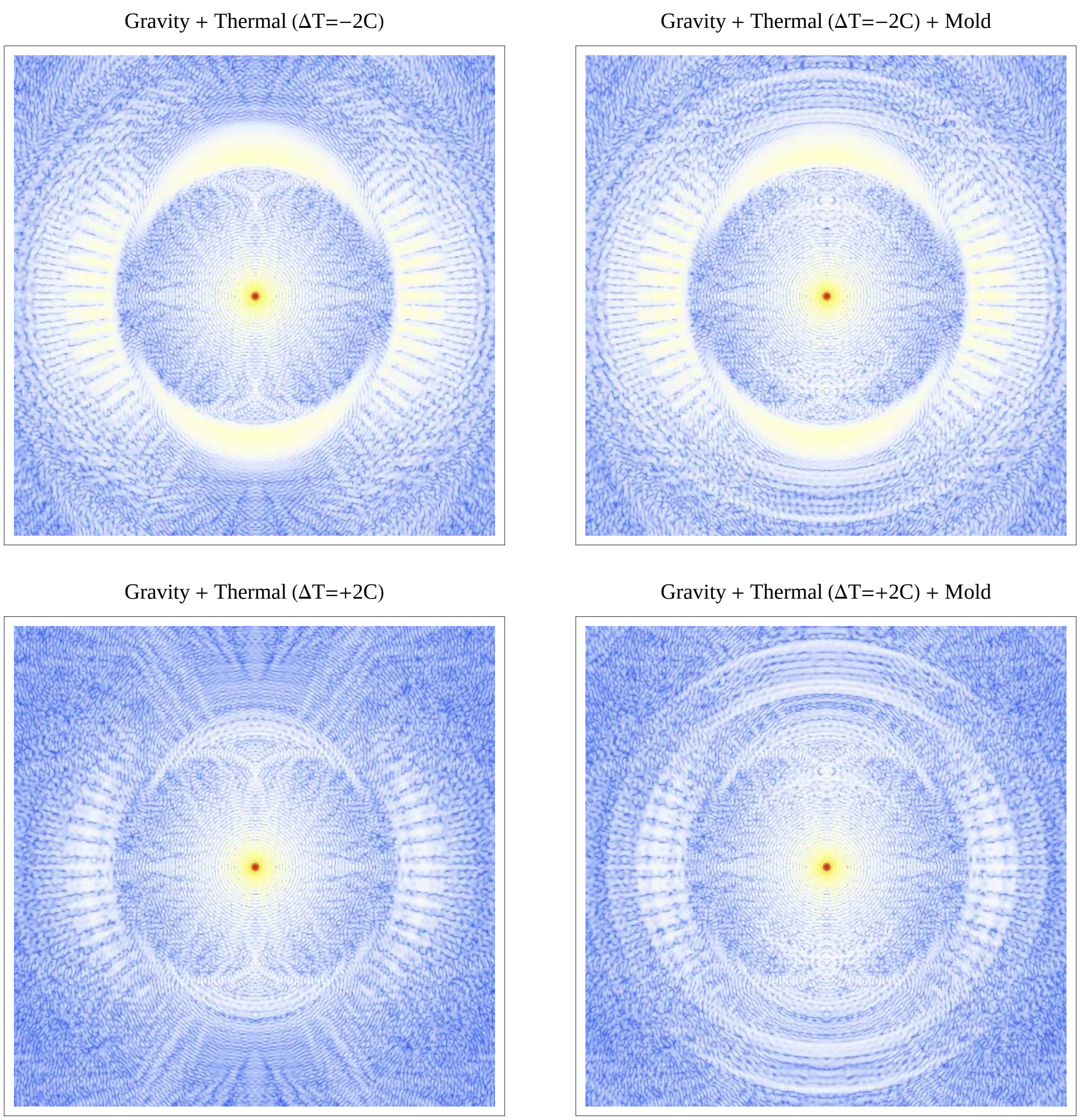

Figure 12. Simulations of the GBT beam pattern at 45 GHz and 44° elevation, using the same 14-dB edge taper as is characteristic of the standard GBT corrugated horns. The beam area shown here is (approximately) $33' \times 33'$.

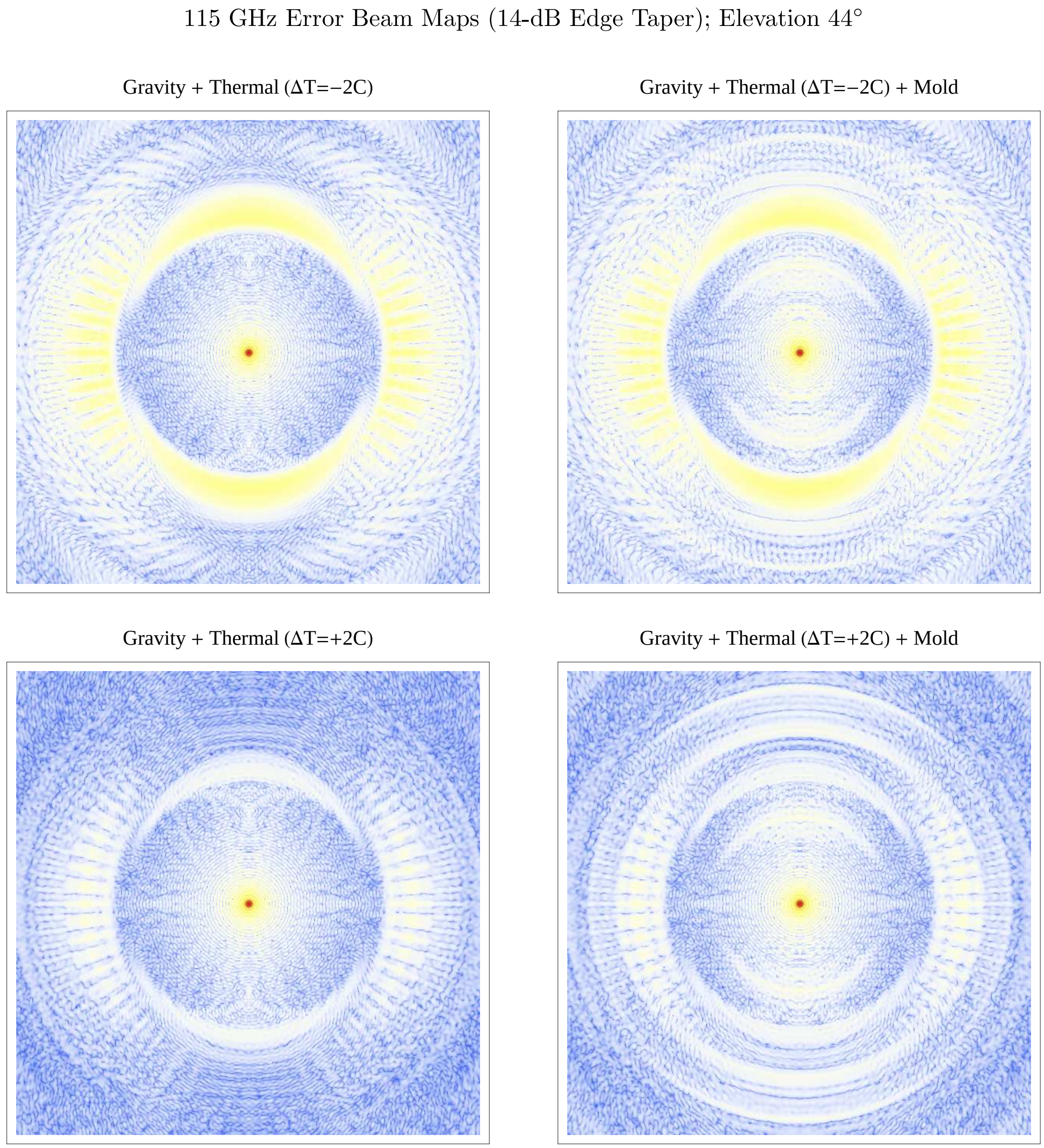

Figure 13. Simulations of the GBT beam pattern at 115 GHz and 44° elevation, using a 14-dB edge taper. The beam area shown here is (approximately) $13' \times 13'$.

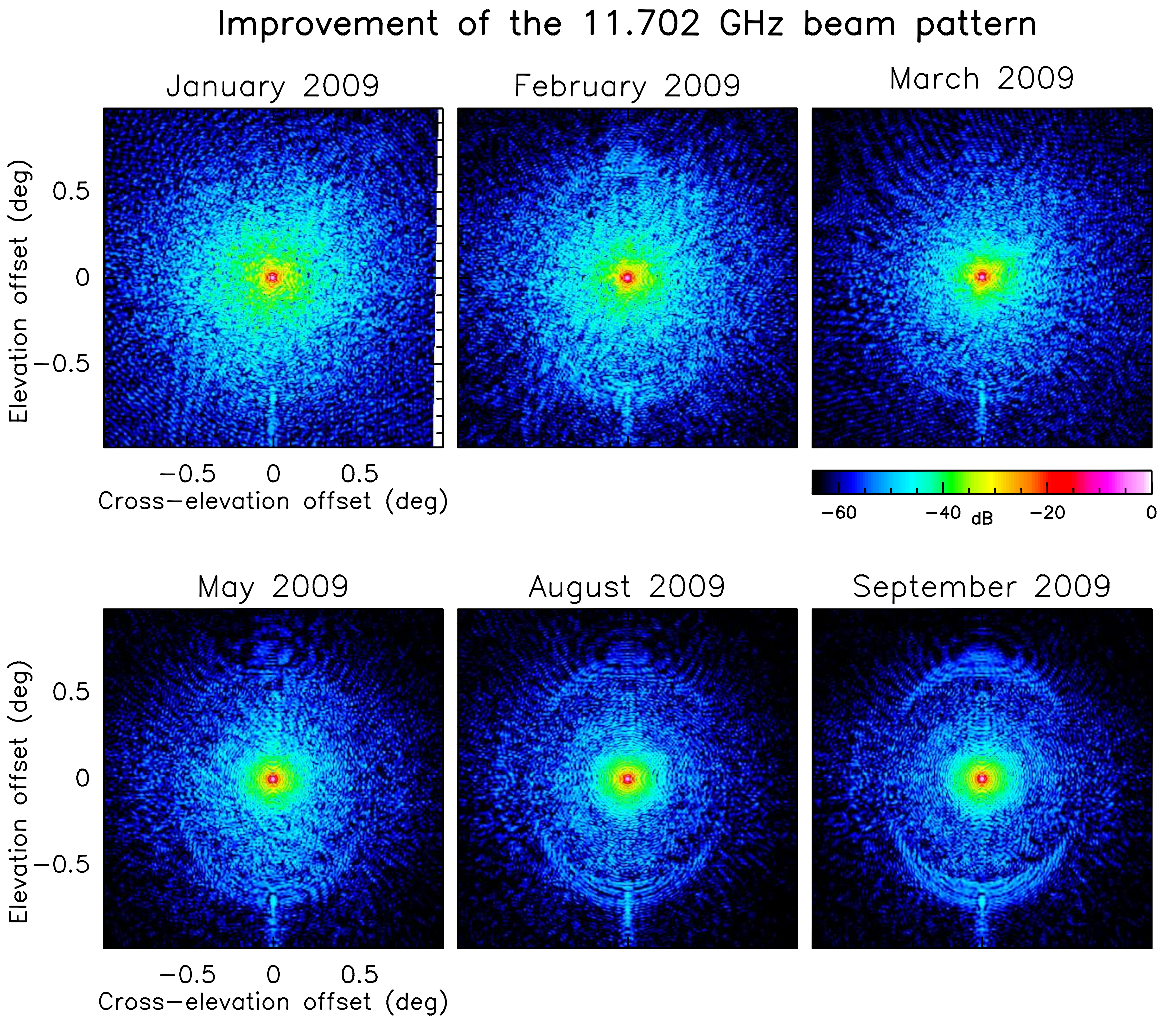

Figure 14. Improvement of the measured 11.7 GHz cross-correlated amplitude beam pattern with successive iterations of holographic mapping and actuator zero-point readjustment. Note the emergence of the partial-arc artifacts near elevation offsets $\pm 0\overset{\circ}{.}6$. Also, compare with the model beam maps of Figures 3, 7, and 10.

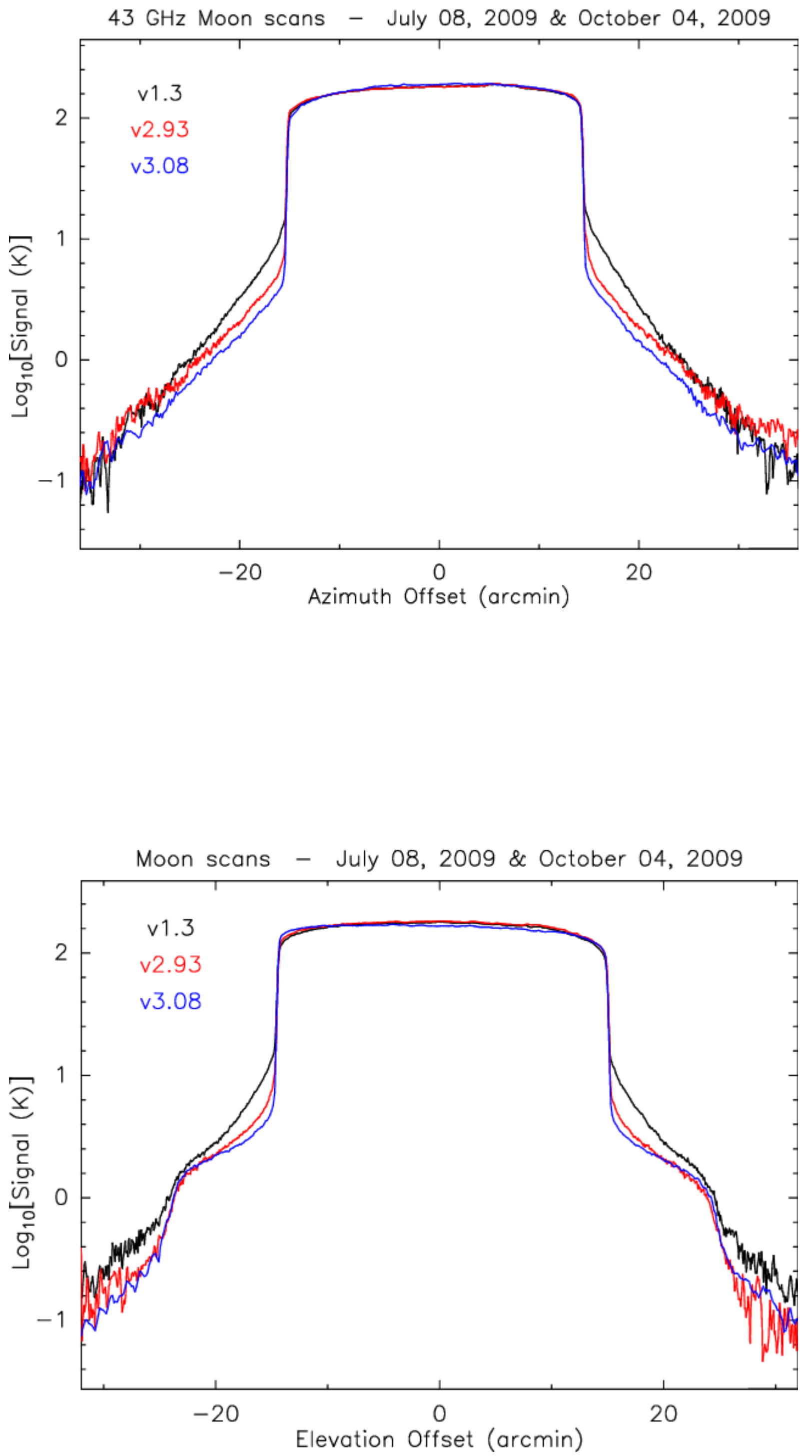

Figure 15. Lunar scans taken at Q-band (43 GHz) showing improvement with successive surface adjustments. The shoulders seen in the elevation scans *(Lower plot)* correspond to the pair of partial-arc artifacts evident in the holography map displays of Figure 14.

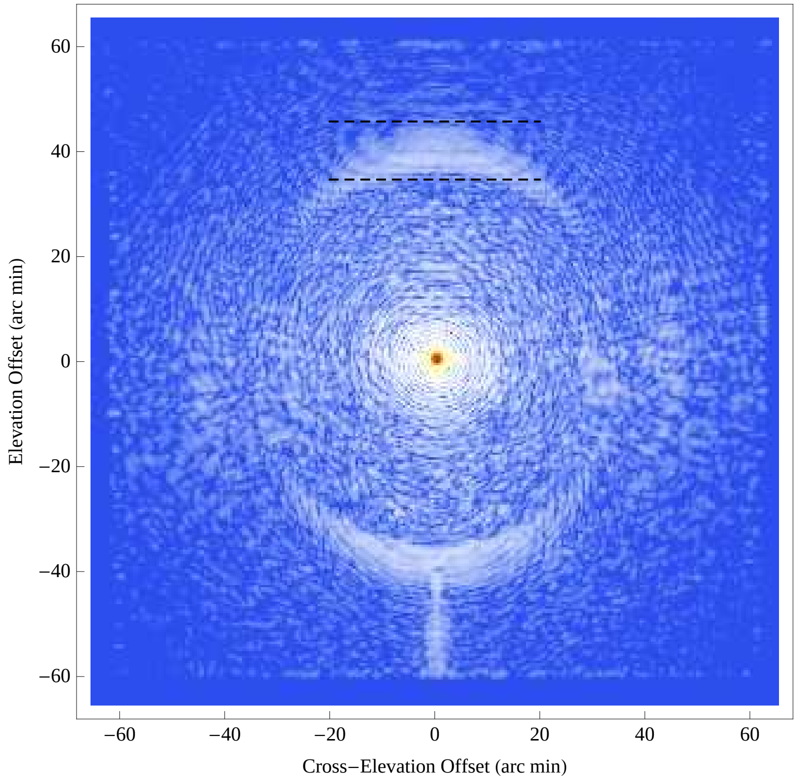

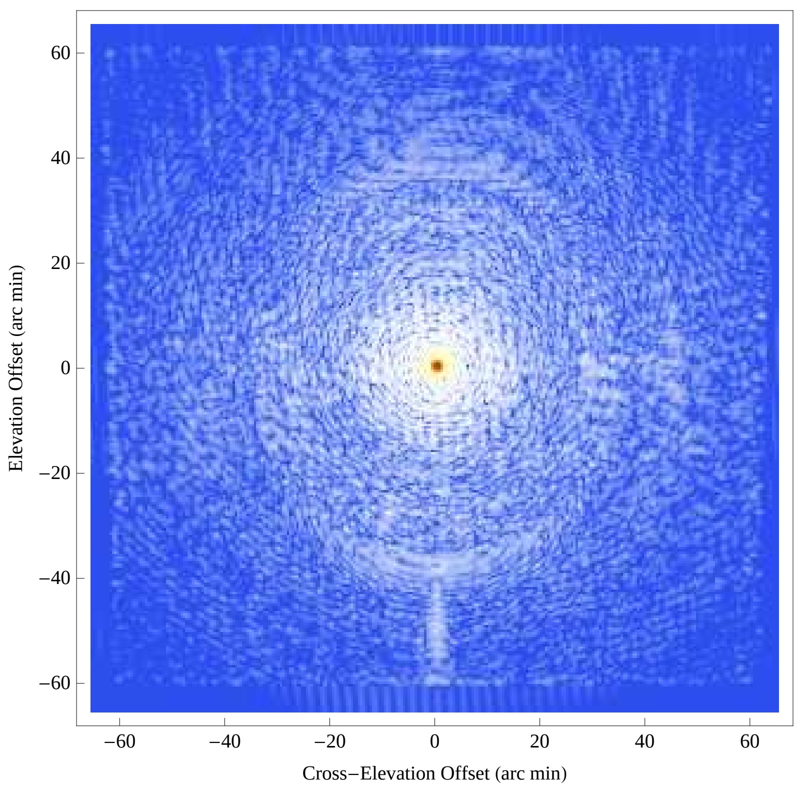

Figure 16. *(Top)* Sept. 11, 2009, nighttime holography beam map. From thermal sensors mounted on the backup structure and panel skin near hoop 16+000 a mean thermal gradient $\overline{\Delta T} = -2.69\,^\circ\mathrm{C}$ was observed; and at hoop 36+000, $\overline{\Delta T} = -3.21\,^\circ\mathrm{C}$. The dashed lines delineate a certain zone defined in §7.1 of the text. *(Bottom)* Jan. 21, 2010, nighttime beam map acquired under conditions of very stable air temperature ($\overline{\Delta T} = -0.45\,^\circ\mathrm{C}$ at 16+000, but no data at 36+000) and excellent phase stability. The two prominent arc-like artifacts appear significantly diminished in the lower display, suggesting that panel thermal gradients dominate over gravitational distortion.

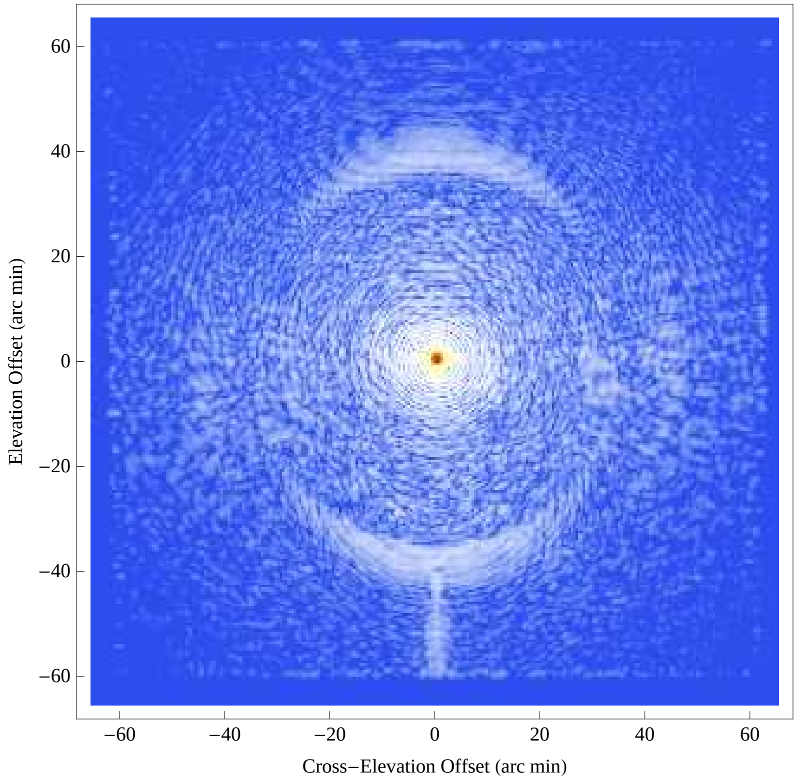

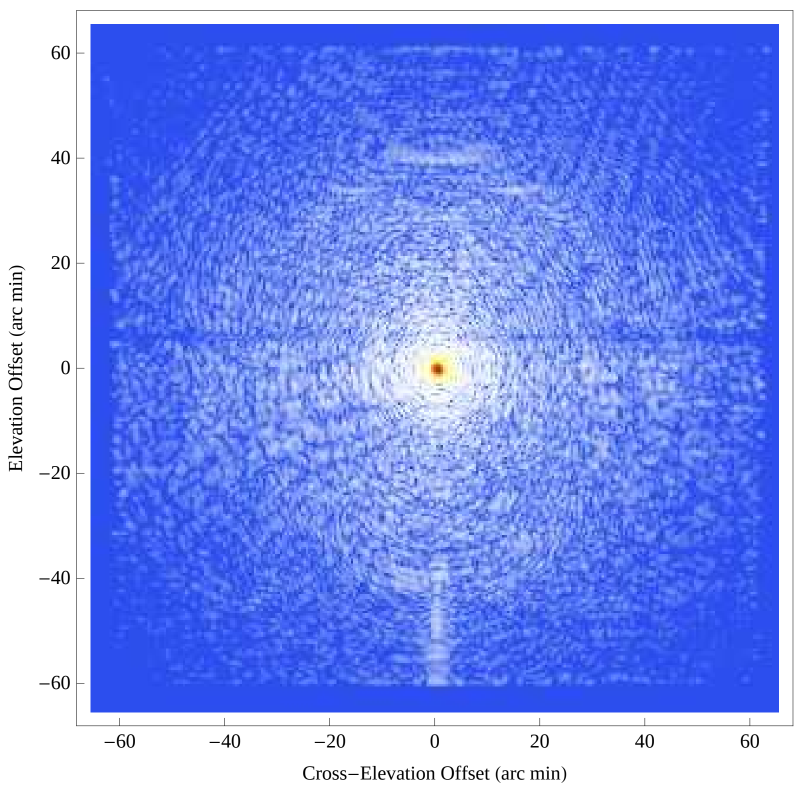

Figure 17. *(Top)* Sept. 11, 2009, nighttime holography beam map (same as shown in previous figure). At hoop 16+000 a mean thermal gradient $\overline{\Delta T} = -2.69\,^{\circ}\mathrm{C}$ was observed; and at hoop 36+000, $\overline{\Delta T} = -3.21\,^{\circ}\mathrm{C}$. *(Bottom)* Nov. 21, 2009, daytime holography beam map acquired under sunny conditions, between 08:30 and 12:30 local time. At hoop 16+000, $\overline{\Delta T} = +5.00\,^{\circ}\mathrm{C}$ (no data at 36+000). Note the near disappearance of the the partial arc features, evidence that positive thermal gradients may sometimes act to largely cancel out the gravitational distortion.

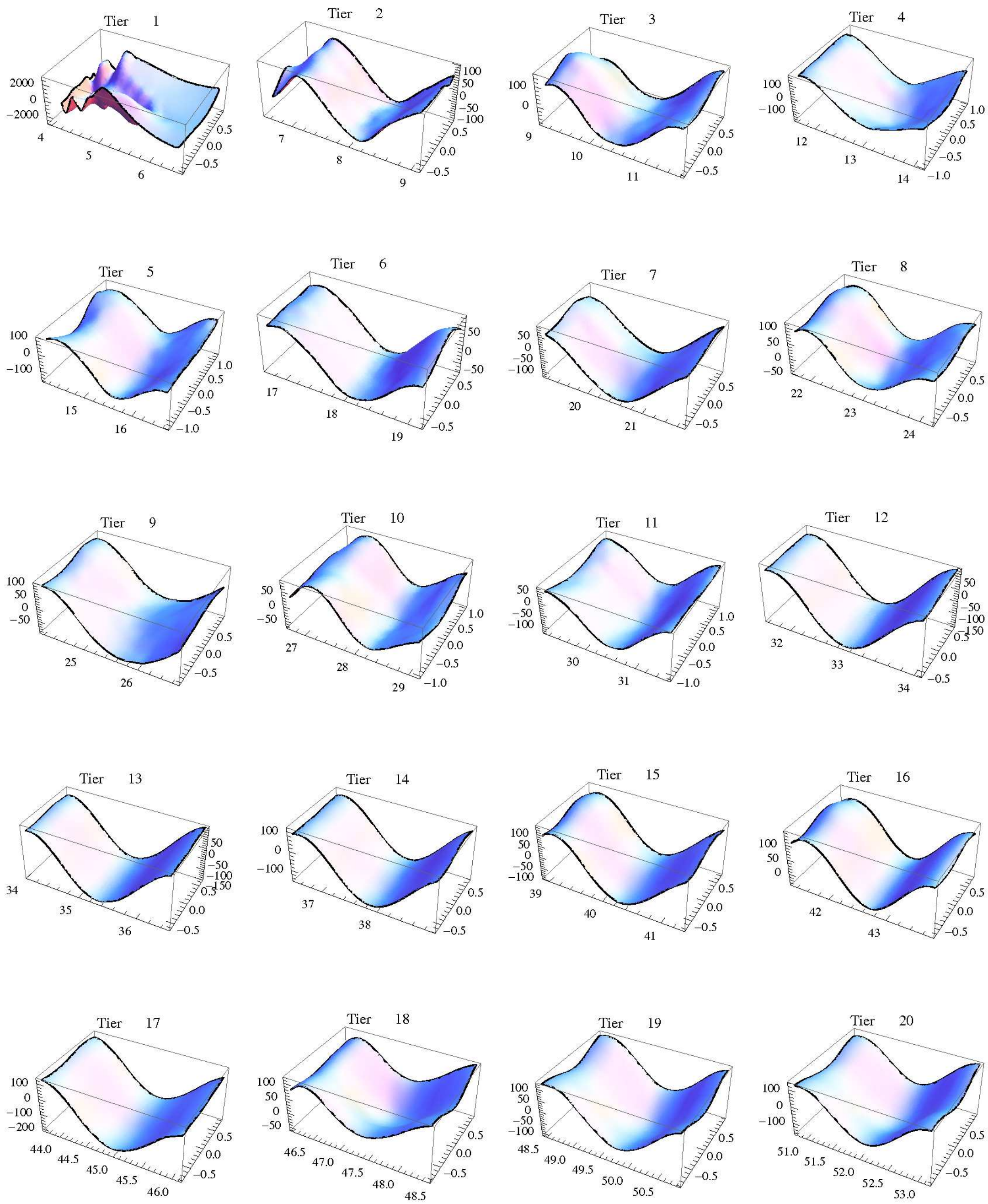

Figure 18. Tier-average profiles of the GBT primary surface error derived from the Sept. 11, 2009, holography map, acquired during nighttime using the Galaxy 28 satellite beacon, at elevation 44°. The map was ring-filtered, as usual, and high-pass filtered by removal of 55 Zernike terms. The Tier 3 through Tier 42 average profiles—i.e., all tiers but the innermost two and outermost two—all show a prominent central central depression, probably representative of a combination of gravitational sag and negative thermal gradients through the panels. And the tier-average profiles appear to more resemble the patterns of thermal deformation (Fig. 6) than those of gravitational sag (Fig. 2). *(Continued on next page.)*

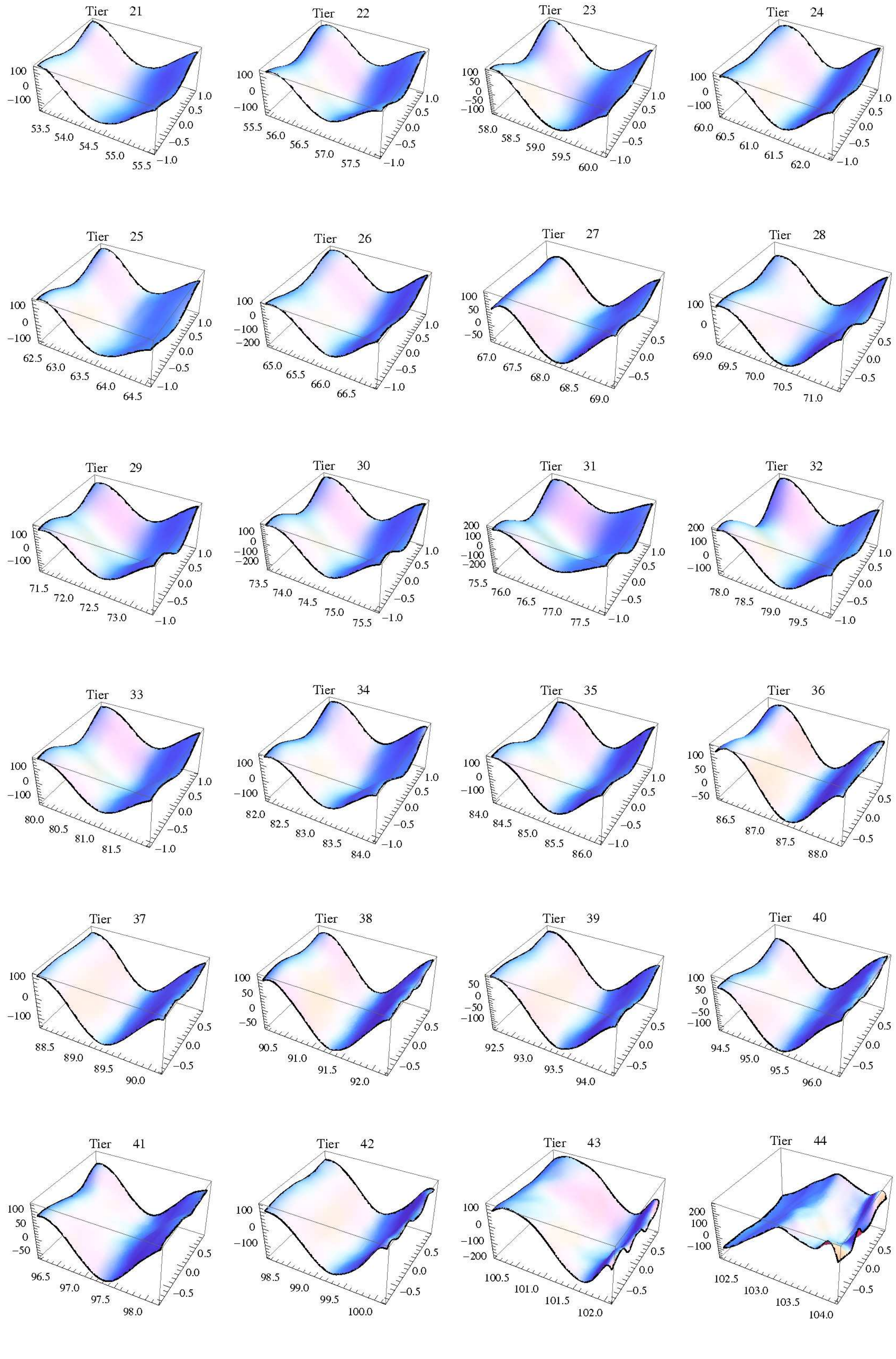

Figure 18 *(Continued)***.** Tier-average profiles for Tiers 21–44 are shown above.

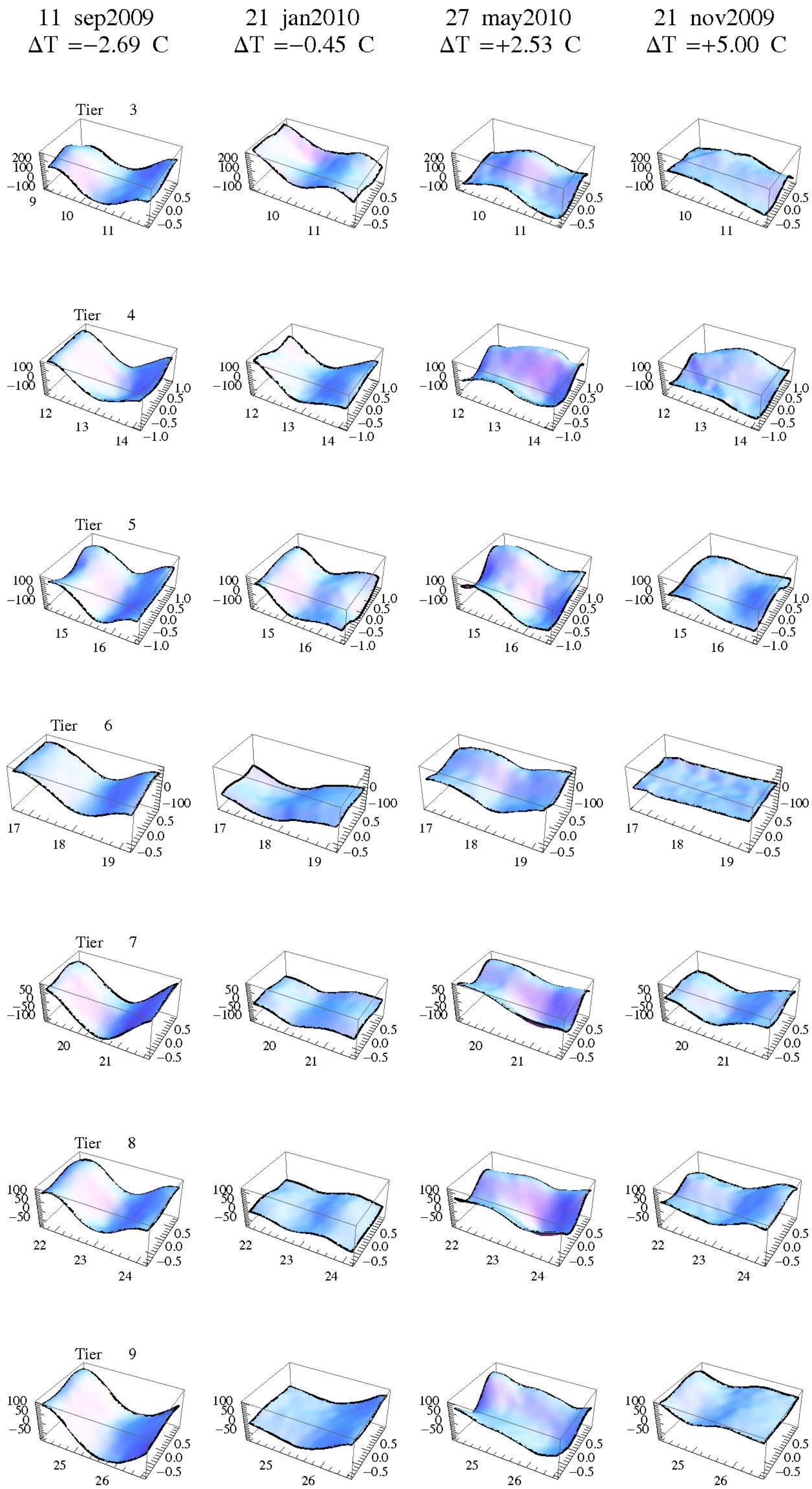

Figure 19. Comparison of tier-average panel profiles for holography maps taken on four different dates. The mean temperature gradient during each map (measured between the panel skin and a nearby BUS member, at the center of Tier 16) is noted in the column headings. *(Continued on next page.)*

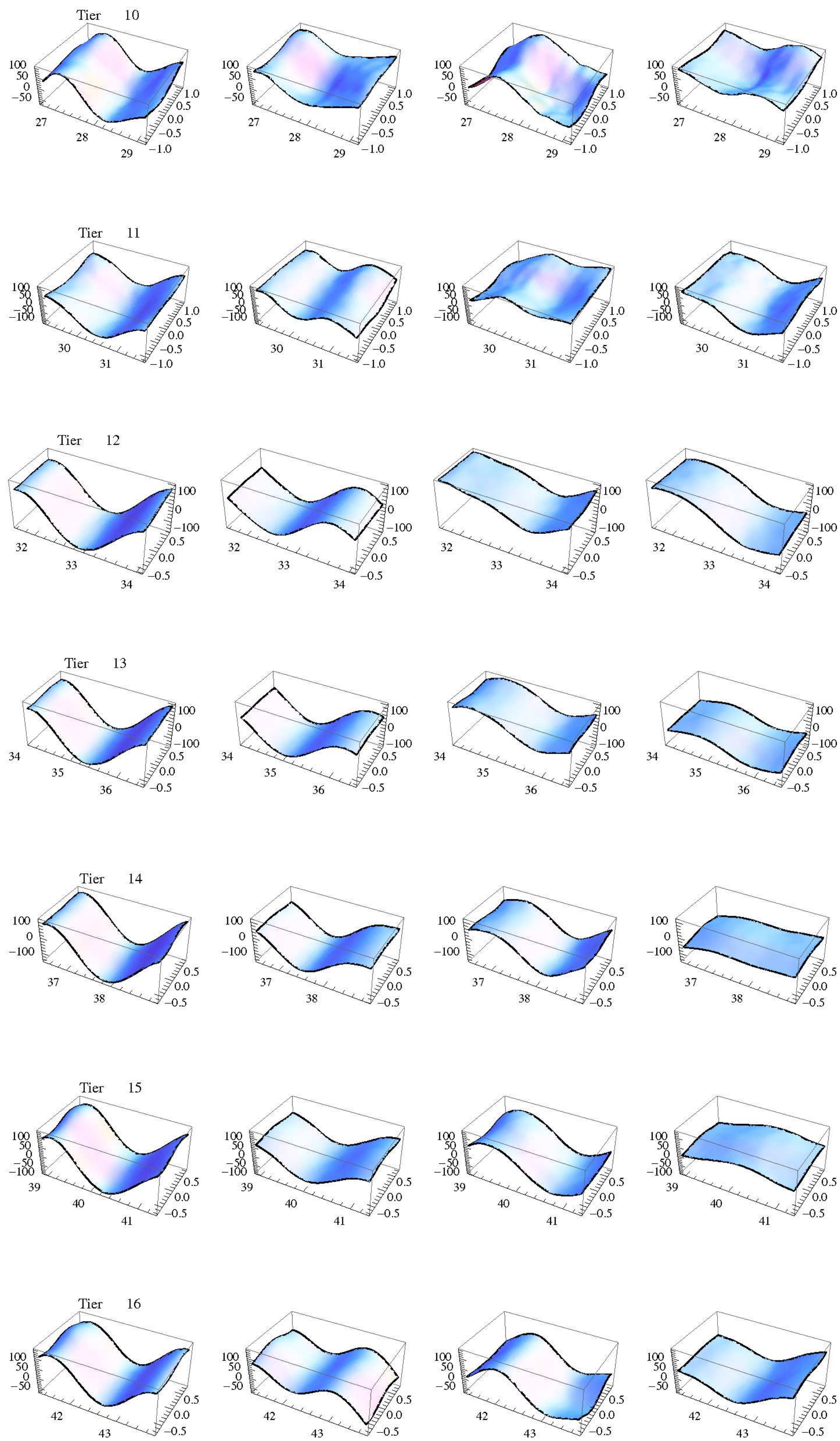

Figure 19 *(Continued)***.** Tiers 10–16. *(Continued on next page.)*

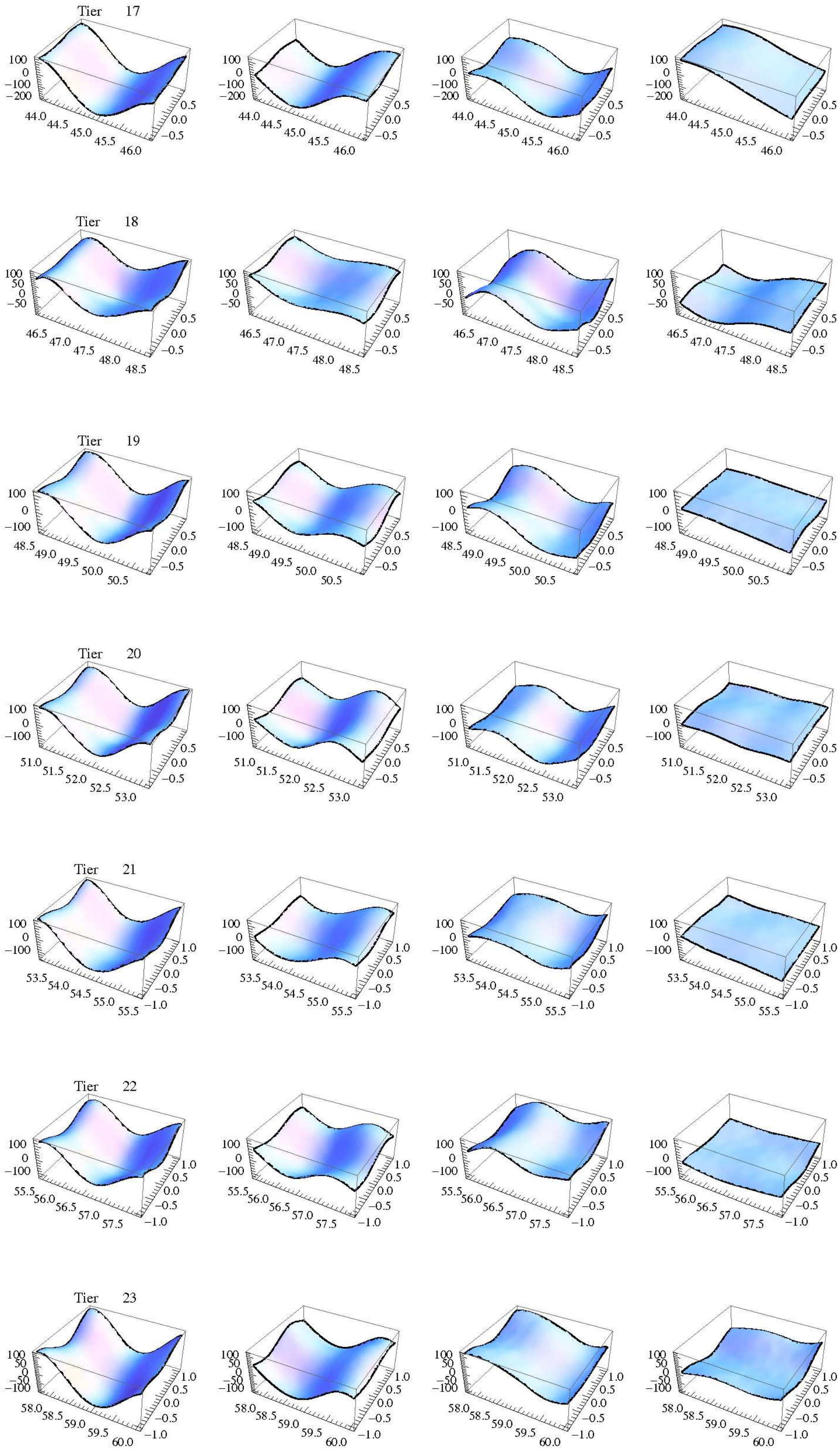

Figure 19 *(Continued)*. Tiers 17–23. *(Continued on next page.)*

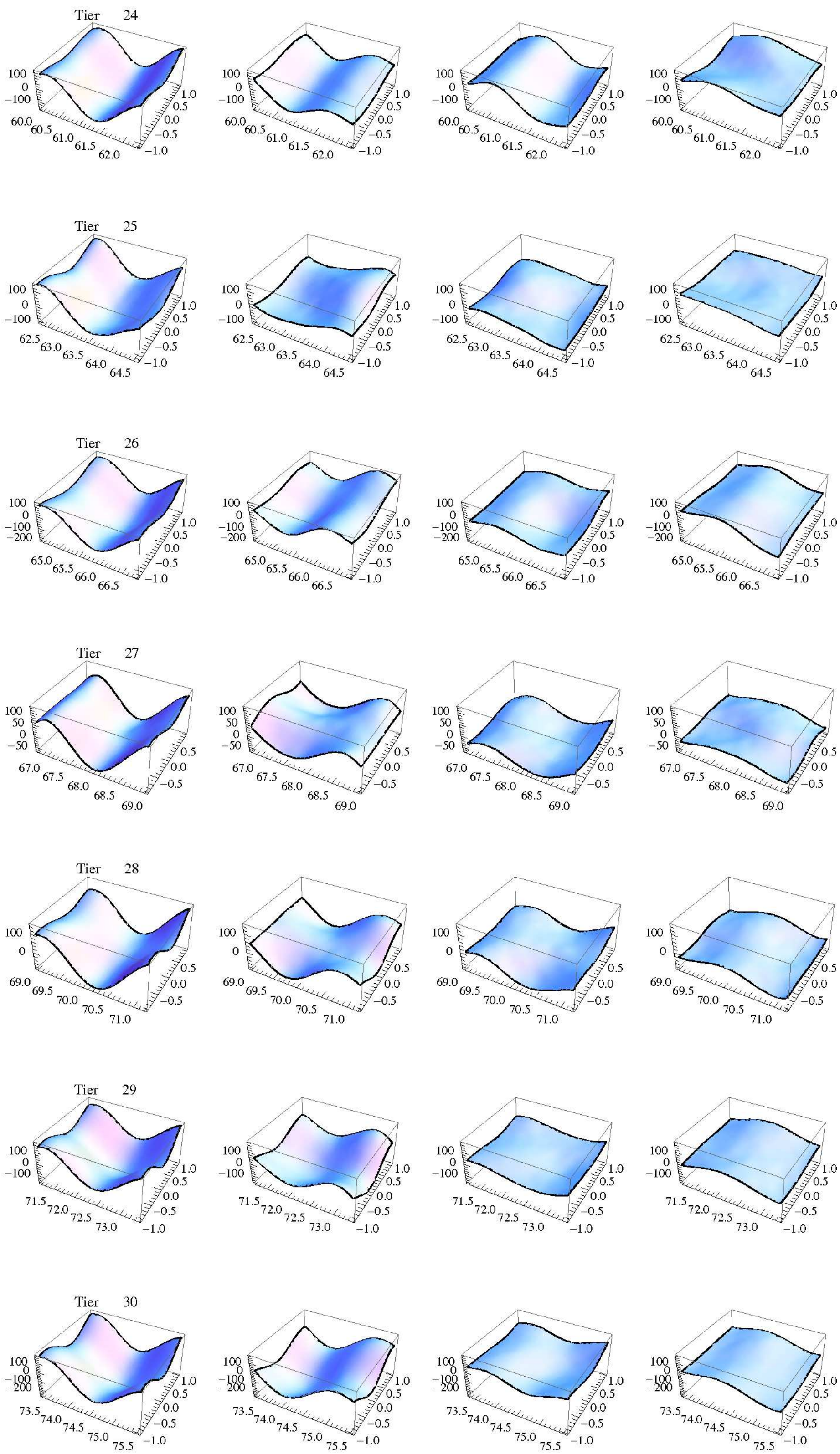

Figure 19 *(Continued)*. Tiers 24-30. *(Continued on next page.)*

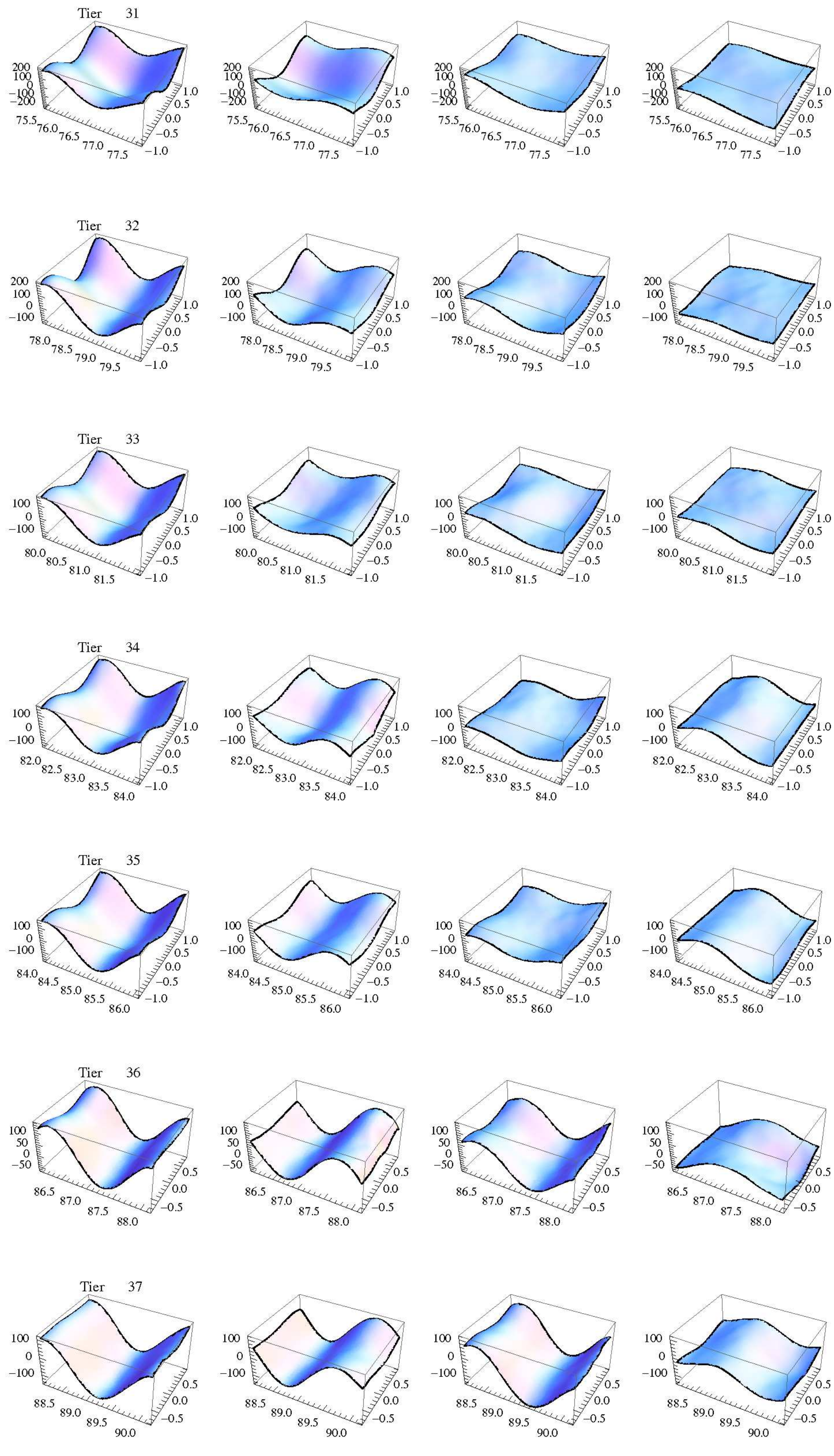

Figure 19 *(Continued)***.** Tiers 31–37. *(Continued on next page.)*

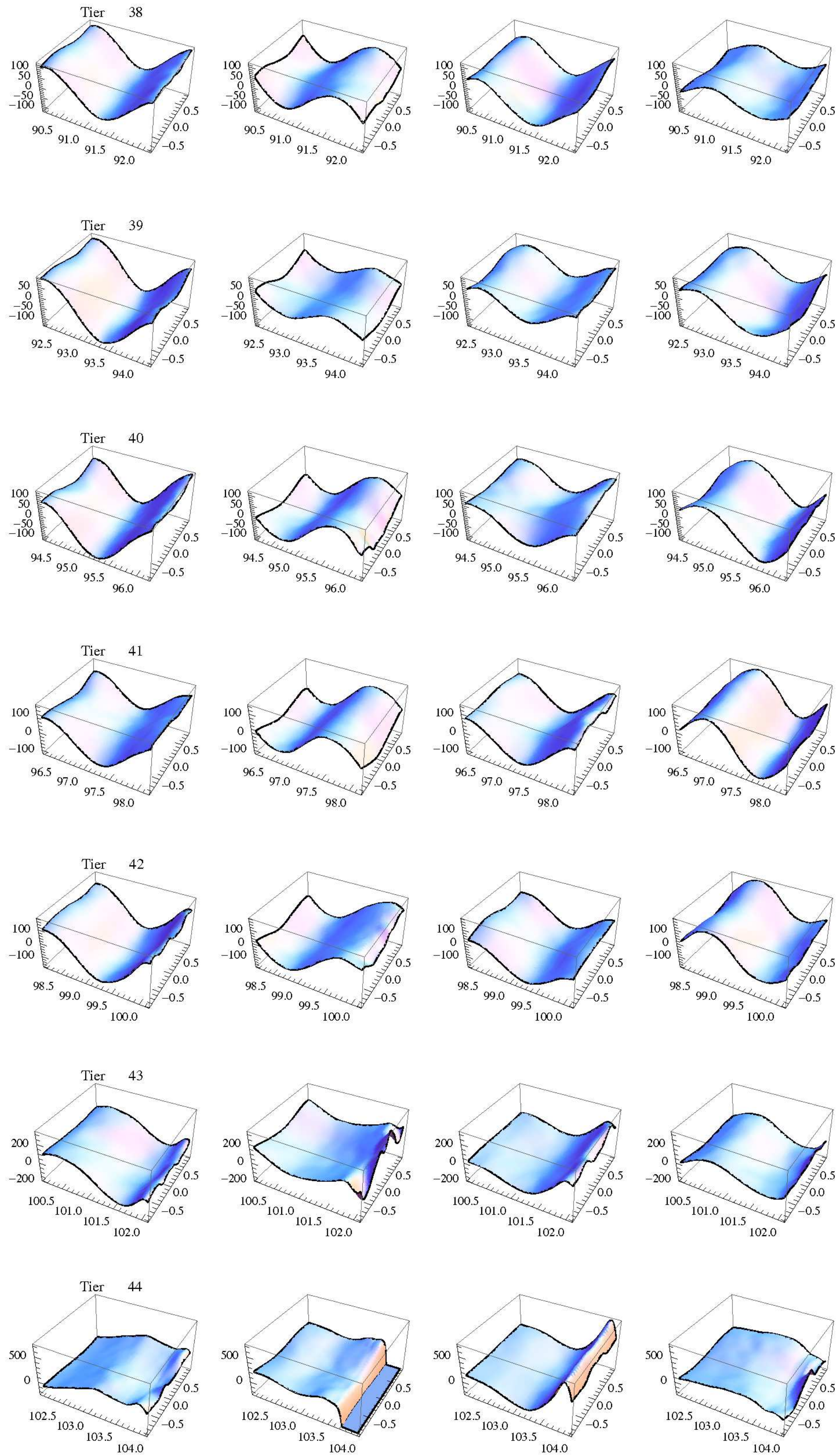

Figure 19 *(Continued)***.** Tiers 38–44.

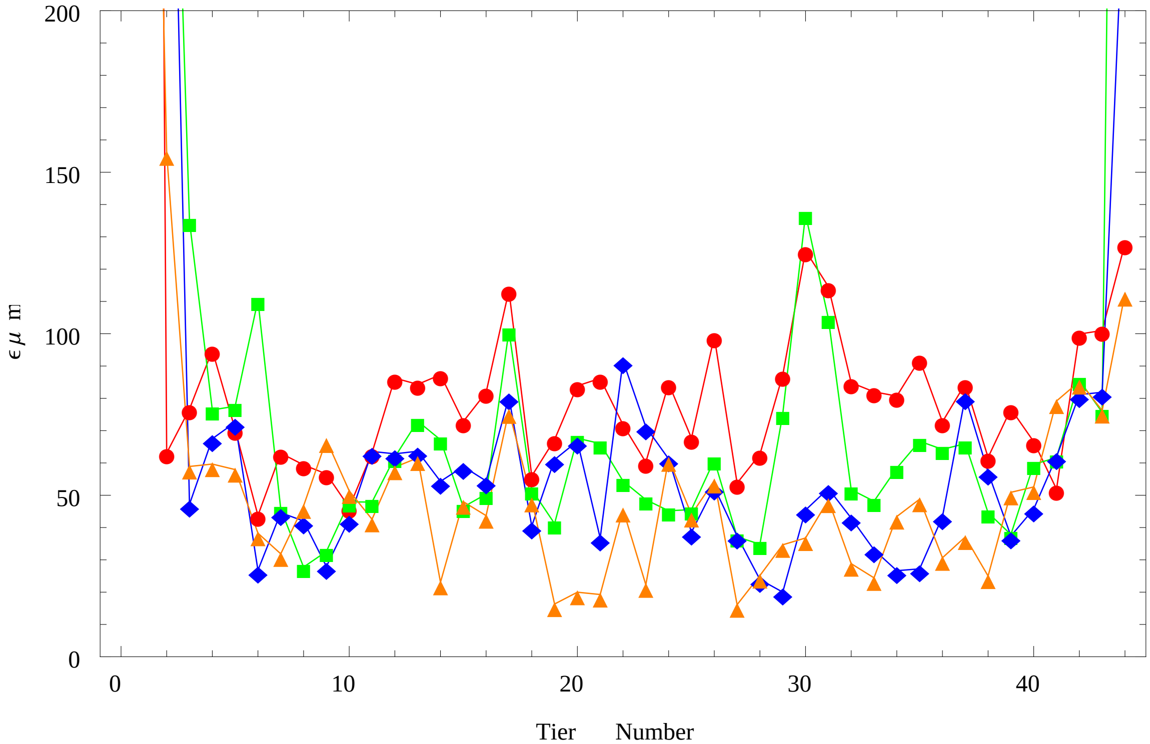

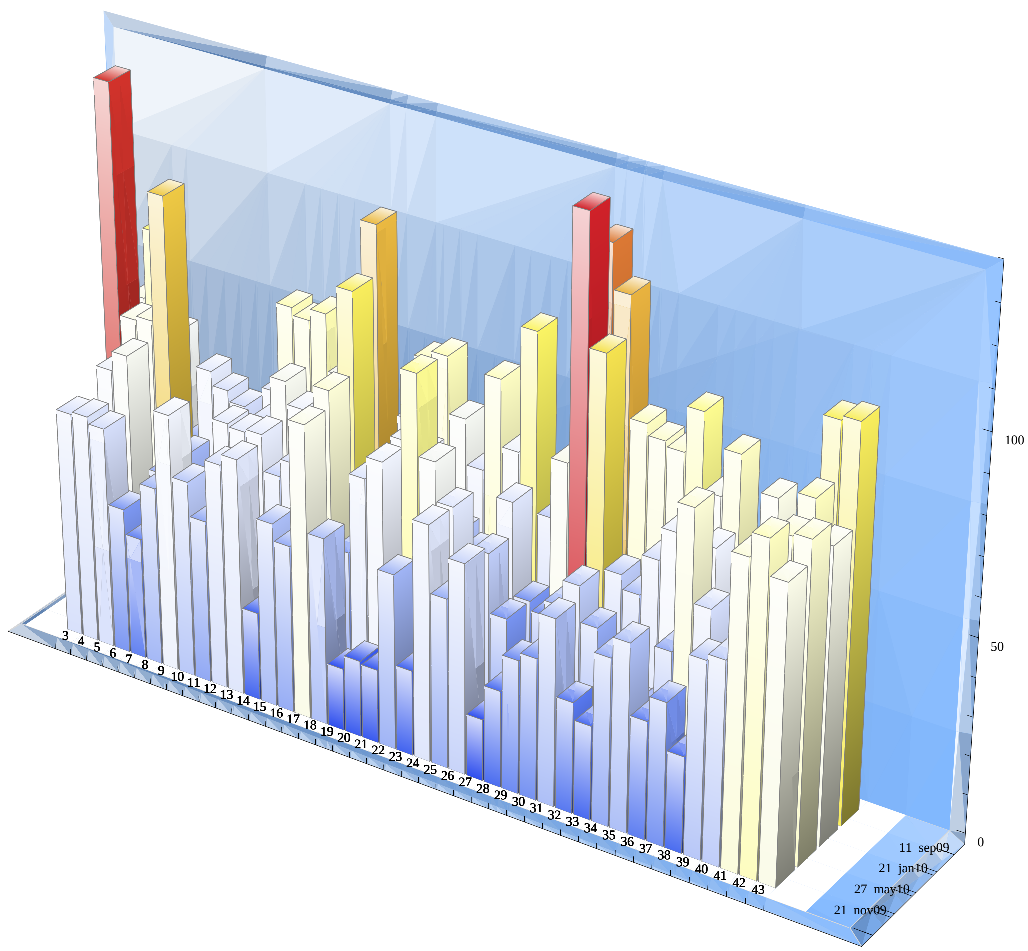

Figure 20. *(Top)* Tier-average panel r.m.s.'s for the four sets of data shown in Figure 19: (Red) Sept. 11, 2009; (Green) Jan. 21, 2010; (Blue) May 27, 2010; (Orange) Nov. 21, 2009. *(Bottom)* Bar chart showing the tier-average panel r.m.s.'s for the four sets of data (Tiers 3–43 only).

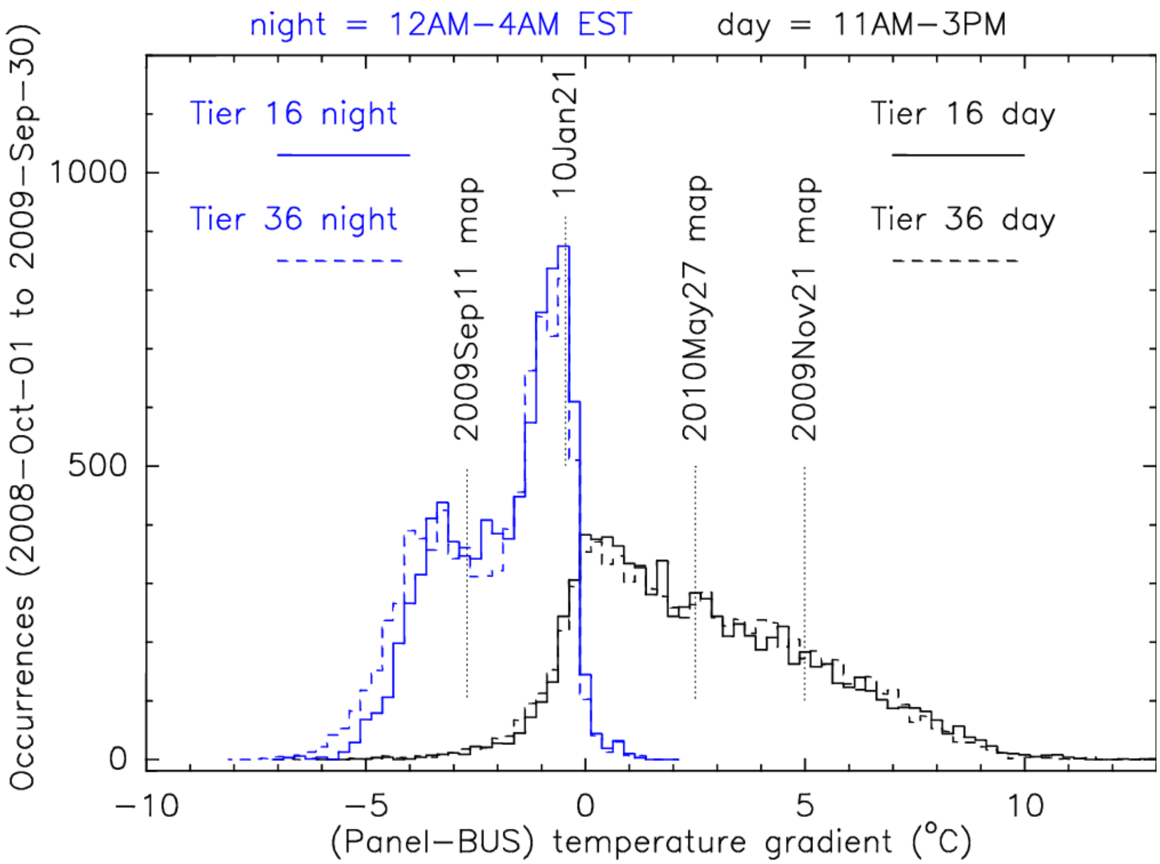

Figure 21. Paired thermal sensors were mounted on the backside of the panel skin and on an adjacent BUS member, at a panel near the center of Tier 16 and on another near the center of Tier 36. Data from these sensors were recorded nearly continuously from Oct. 1, 2008, through Sept. 30 of the following year. This plot shows histogram envelopes of the 10-minute median temperature differences observed during the four-hour nighttime period, midnight to 4AM EST, and during the daytime period 11AM–3PM. The quartile values of the inferred temperature gradients are at node 16+000, $(-2.68, -1.44, -0.62)\,^{\circ}\mathrm{C}$ (nighttime) and $(0.67, 2.36, 4.60)\,^{\circ}\mathrm{C}$ (daytime); and at node 36+000, $(-3.22, -1.65, -0.73)\,^{\circ}\mathrm{C}$ (nighttime) and $(0.68, 2.43, 4.61)\,^{\circ}\mathrm{C}$ (daytime). Note the apparent bimodality of the nighttime ΔT distributions. The left-hand peak likely corresponds to predominantly clear-sky conditions, and the right-hand one to overcast. The implication for high-frequency (e.g., 3-mm) observing is that, when atmospheric transparency is at its best, the surface efficiency is likely sub-optimal, because gravitational and thermal distortion of the panels act in the same direction.

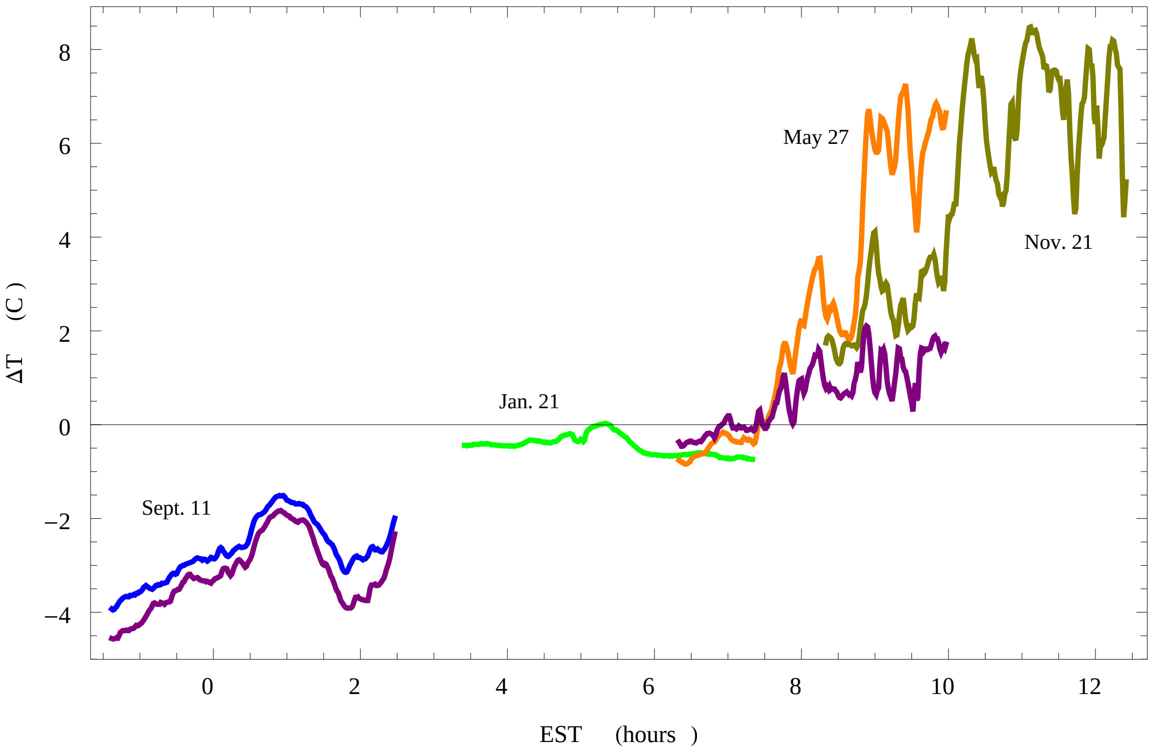

Figure 22. Temperature gradients ($\Delta T = T_{\mathrm{skin}} - T_{\mathrm{BUS}}$) measured at surface node 16+000 vs. time of day, during the acquisition of the Sept. 11, 2009 *(Blue)*, Nov. 21, 2009 *(Olive)*, Jan. 21, 2010 *(Green)*, and May 27, 2010 *(Orange)*, holography data. Data at an additional node, 36+000—shown by the two purple curves—were recorded during the Sept. 11 and May 27 observing sessions. For the May 27 run the purple curve represents $T_{\mathrm{skin}} - T_{\mathrm{rib}}$ rather than $T_{\mathrm{skin}} - T_{\mathrm{BUS}}$ (see text for further discussion). Compare with Figure 21.

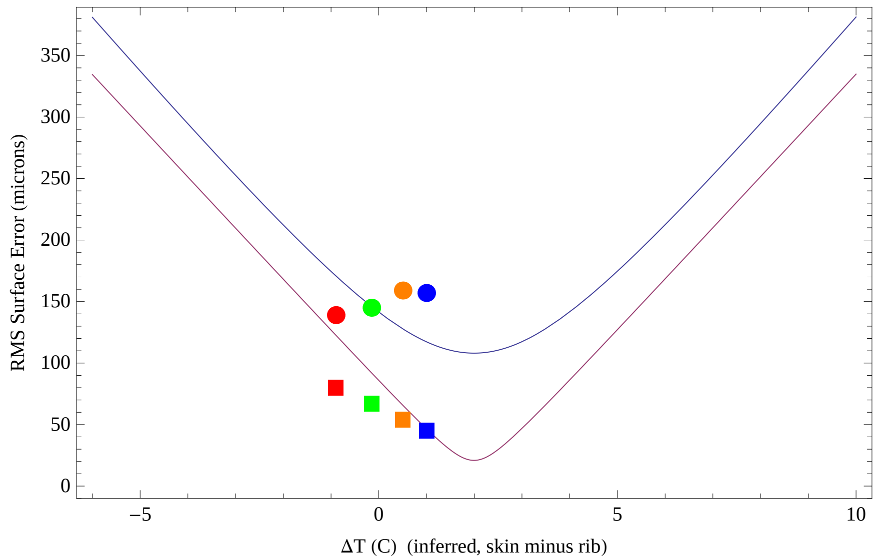

Figure 23. The lower curve, shown in purple, represents the predicted small-scale surface error due to the combined effects of panel thermal gradients and gravity, for elevation 44°, plotted vs. thermal gradient ΔT (assuming the same ΔT through each panel). At this elevation, the thermal and gravitational error components should nearly cancel when $\Delta T \approx 2\,^{\circ}$C, according to our model. The upper curve, in blue, includes allowances for other sources of small-scale error; here we assume $75\,\mu$m r.m.s. primary panel manufacturing error, $50\,\mu$m r.m.s. panel setting error, and $70\,\mu$m r.m.s. subreflector surface error. The filled circles represent the median absolute deviation (MAD) about the median residual in our holography maps, scaled by a factor 1.48. (Unlike the r.m.s., the MAD estimator is very insensitive to outliers; for normally distributed data, the expectation of the MAD, scaled by a factor ∼1.48, is equal to the standard deviation. So here we use the scaled MAD as a proxy for the r.m.s.) The medium- and large-scale surface errors have been filtered out of the holography data by subtraction of the best-fit Zernike polynomial model. The red, green, and blue points correspond to the Sept. 11, 2009, Jan. 21, 2010, and Nov. 21, 2009, holography maps. The colored rectangles represent the σ_{aperture} values computed via Equation 1.

Ideally, the abscissae in the plot should be ΔT *values defined according to* $\Delta T = T_{\text{skin}} - T_{\text{rib}}$ *rather than* $\Delta T = T_{\text{skin}} - T_{\text{BUS}}$*. However, prior to May 2010, only* T_{skin} *and* T_{BUS} *measurement sensors were available. So here we use the node 16+000* $T_{\text{skin}} - T_{\text{BUS}}$ *values, scaled by a factor* $k = 1/3$ *for a nighttime map or* $k = 1/5$ *for a daytime map. (See Section 8 of the text for further discussion.)*

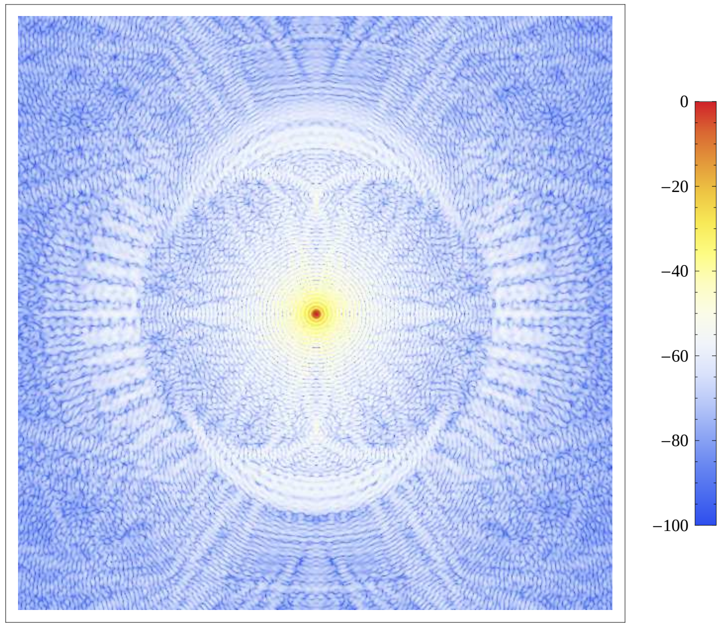

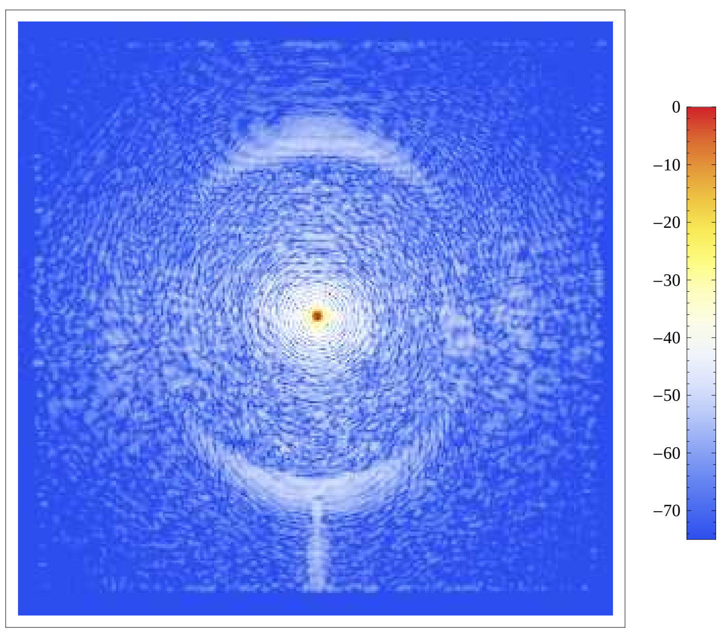

Figure 24. Plot legends were not included in previous figures. Here we show: *(Top)* the gravity, plus thermal ($\Delta T = 2\,^\circ$C), plus mold theoretical beam pattern of Fig. 10, together with a legend representing the minus 100 dB to 0 dB intensity transfer function used in display of all the model beam maps (Figs. 3, 7, and 9–13); and *(Bottom)* the Sept. 11, 2009, holography beam map of Fig. 16, with the appropriate legend for the −75 dB to 0 dB transfer function used for the previous holography beam map displays (Figs. 16 and 17). (Note that the latter maps have a higher noise floor than the models.)